

1 **Title:** Structural Insights into Ligand Recognition, Selectivity and Activation of the
2 human Bombesin Receptor Subtype-3

3
4 Changyao Li^{1,2,3,8}, Youwei Xu^{1,8}, Xinheng He^{1,4}, Wenxin Su^{5,6}, Jingru Li⁷, Xinzhu Li⁷, H. Eric
5 Xu^{1,2,3,4,7,9*}, Wanchao Yin^{6,1,4,5,9*}

6
7 ¹The CAS Key Laboratory of Receptor Research, Shanghai Institute of Materia Medica,
8 Chinese Academy of Sciences, Shanghai 201203, China

9
10 ²Lingang Laboratory, Shanghai 200031, China

11
12 ³School of Life Science and Technology, ShanghaiTech University, Shanghai 201210,
13 China

14
15 ⁴University of Chinese Academy of Sciences, Beijing 100049, China

16
17 ⁵Guangzhou University of Chinese Medicine, Zhongshan Institute for Drug Discovery,
18 Guangdong 510000, China

19
20 ⁶Zhongshan Institute for Drug Discovery, Shanghai Institute of Materia Medica,
21 Chinese Academy of Sciences, Guangdong 528400, China

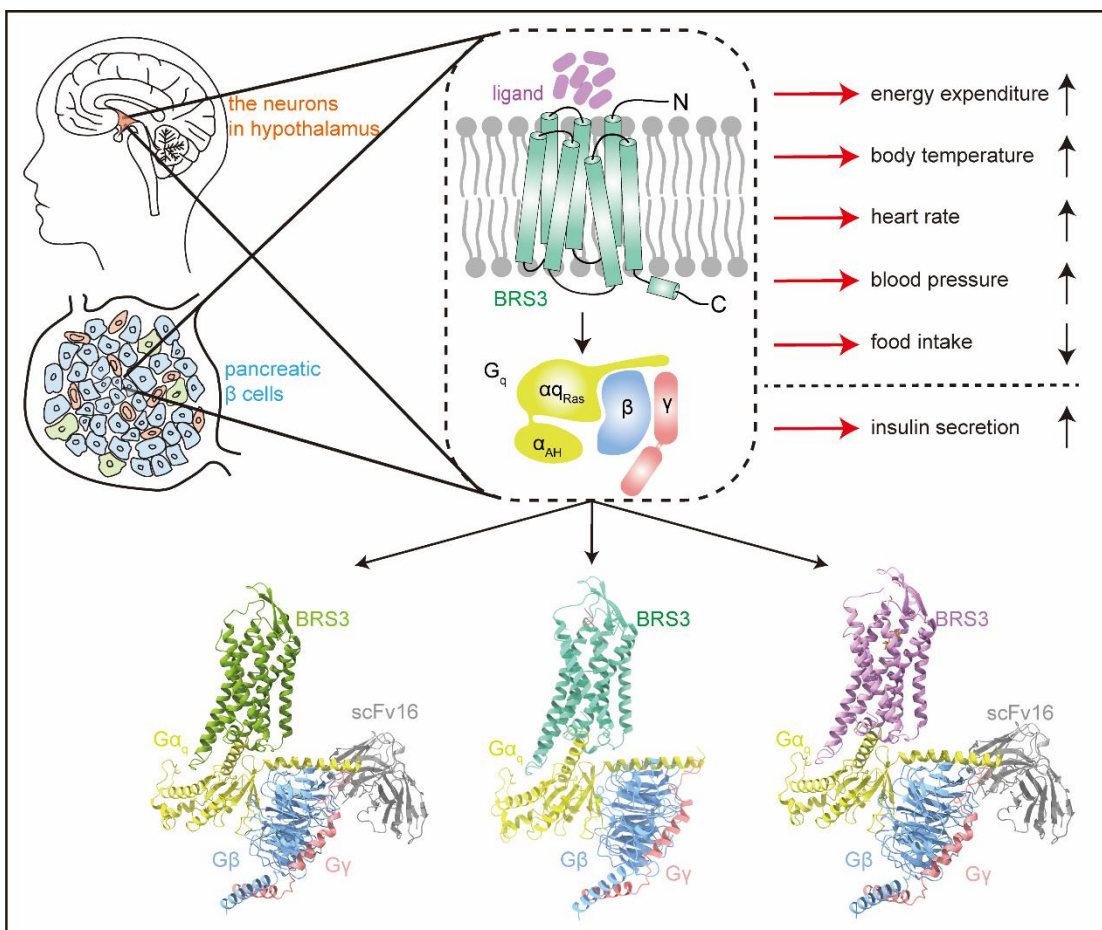
22
23 ⁷School of Chinese Materia Medica, Nanjing University of Chinese Medicine, Nanjing
24 210023, China

25
26 ⁸These authors contributed equally

27
28 ⁹Lead Contact

29
30 *Correspondence: eric.xu@simm.ac.cn (H.E.X), wcyin@simm.ac.cn (W.Y.)

32 **Graphical Abstract**



33

34 **In Brief**

35 Molecular basis for recognition of exogenous agonists by the human bombesin
36 receptor subtype-3 provides avenues for design of new modulators for diabetes and
37 obesity.

38

39 **Highlights**

- 40 • Structures of BRS3-G_q complexes, both in the absence (apo-form) and
41 presence of the ligands BA1 and MK-5046, were determined.
42 • The important residues in the ligand binding pocket for bombesin receptor
43 subtype-3 activation were described.
44 • The basis for ligand selectivity of bombesin receptors was depicted in detail.
45 • Resolution of the binding pockets provides path for rational drug design against
46 bombesin receptor subtype-3 for the treatment of diabetes and obesity.

47

48 **SUMMARY**

49 Bombesin receptor subtype-3 (BRS3) is an important orphan G protein-coupled
50 receptor that regulates energy homeostasis and insulin secretion. As a member of the
51 bombesin receptor (BnR) family, which includes neuromedin B receptor (NMBR) and
52 gastrin-releasing peptide receptor (GRPR), the lack of known endogenous ligands and
53 high-resolution structure has impeded understanding of BRS3 signaling and function.
54 Here, we present cryogenic electron microscopy (cryo-EM) structures of BRS3 in
55 complex with heterotrimeric G_q protein in three states: apo, bound to the pan-BnR
56 agonist, BA1, and bound to the synthetic BRS3-specific agonist MK-5046. These
57 structures reveal the architecture of the orthosteric ligand pocket underpinning
58 molecular recognition. Comparisons with BnR members provide insights into the
59 structural basis for BRS3's selectivity and low affinity for bombesin peptides.
60 Examination of conserved micro-switches suggests a shared activation mechanism
61 among BnRs. Together our results enable deeper exploration of BRS3's ligand
62 selectivity, signaling, and therapeutic targeting for diabetes and obesity.

63

64 **Introduction**

65 G protein-coupled receptors (GPCRs), pivotal membrane proteins, orchestrate cellular
66 responses to a variety of extracellular stimuli, including peptide ligands. Among these,
67 bombesin, a 14-amino acid peptide originally isolated from the European xenopus
68 laevis (*Bombina bombina*)^{1,2}, stands out. In mammals, bombesin analogs such as
69 neuromedin B (NMB) and gastrin-releasing peptide (GRP) interact with specific
70 receptors in the bombesin receptor (BnR) family³. These receptors are integral to
71 physiological processes in the gastrointestinal tract and central nervous system,
72 influencing aspects like food intake⁴, fear memory consolidation⁵, and itch sensation^{6,7}.
73 Structural studies of NMBR and GRPR with various ligands have shed light on the
74 interactions within the BnR family, enhancing our understanding of their structure-
75 function relationships and aiding in the development of novel therapeutics for BnR-
76 related conditions, including cancers and pruritus^{8,9}.

77

78 Bombesin receptor subtype-3 (BRS3), also a member of the BnR family, is an orphan
79 GPCR primarily found in the brain. Unlike its counterparts NMBR and GRPR, BRS3
80 does not exhibit high affinity for the known endogenous bombesin family
81 peptides^{3,10,11}(Table S1), and its natural ligand remains elusive. Despite this, specific
82 ligands have been identified for BRS3. Among them, the synthetic bombesin analog
83 [D-Phe⁶, β-Ala¹¹, Phe¹³, Nle¹⁴]Bn(6–14) (where D and β indicate Dextro- and β-
84 conformations, respectively), referred to as BA1, exhibits high affinity, binding to all
85 three bombesin family receptors. As a pan-BnR agonist, BA1 is frequently utilized in
86 research as a BRS3 agonist^{12,13}. Nonpeptide agonists like MK-5046 have shown
87 selective BRS3 agonism, enhancing our ability to investigate BRS3's functions^{14,15}.
88 Additional agonists, such as DSO-5a and oridonin, have displayed potent and selective
89 BRS3 activation, suggesting their potential in treating metabolic disorders^{16,17}.
90 Particularly, in comparison with MK-5046, DSO-5a activates peripheral BRS3 to control
91 blood glucose homeostasis while circumventing central effects¹⁸. Additionally, oridonin,
92 derived from Isodon rubescens and commonly employed in Traditional Chinese
93 Medicine¹⁷, exhibits pharmacological activities encompassing hypoglycemic and anti-
94 inflammatory effects¹⁹, as well as anti-cancer effects²⁰. As a novel BRS3 ligand,
95 oridonin holds promise as a lead compound for treating metabolic disorders, including
96 type 2 diabetes and obesity.

97
98 Utilizing these synthetic ligands and animal models has revealed BRS3's critical roles
99 in regulating energy homeostasis, glucose metabolism, and blood pressure. Its
100 significant function in obesity was initially identified²¹, followed by findings underscoring
101 its necessity for energy balance and insulin secretion²²⁻²⁴. BRS3 neurons in the
102 hypothalamus can be activated by cold exposure, refeeding, and certain agonists.
103 Notably, activation of BRS3 neurons in the dorsomedial hypothalamus increased
104 sympathetic nervous tone, elevating energy expenditure, body temperature, heart rate,
105 and blood pressure via brown adipose tissue, heart, and arteries, respectively, without
106 affecting food intake or physical activity. Conversely, the activation of BRS3 neurons

107 in the paraventricular nucleus of the hypothalamus reduced food intake, without
108 affecting energy expenditure, body temperature, or physical activity²⁵ (**Figure 1A**).
109 Additionally, agonists of BRS3 can stimulate insulin secretion from pancreatic β cells
110 (**Figure 1A**), making BRS3 a promising target for metabolic diseases such as obesity
111 and diabetes²⁶. However, the lack of structural data for BRS3, especially in different
112 ligand-bound states, has hindered our understanding its molecular mechanisms and
113 the development of targeted treatments.

114
115 In this study, we present cryo-EM structures of BRS3 in active conformations, both in
116 the absence and presence of ligands (BA1 and MK-5046). Together with mutational
117 studies, these structures elucidate the mechanisms of ligand binding and receptor
118 activation, offering crucial insights into this orphan receptor. This information is
119 invaluable for structure-based drug design targeting BRS3, potentially revolutionizing
120 treatment approaches for obesity, diabetes, hypertension, and related diseases.

121

122 **Results**

123 **Structure determination of BRS3-G_q complexes**

124 For the cryo-EM analysis of BRS3-G_q complexes, we engineered the human BRS3 by
125 attaching a thermostabilized apocytochrome b⁵⁶²RIL (BRIL) to its N-terminus. This was
126 done to enhance the stability and homogeneity of the complex, crucial for effective
127 cryo-EM studies²⁷ (**Figure S2**). Additionally, we utilized the NanoBiT tethering strategy:
128 fusing the large part of NanoBiT (LgBiT) to the C-terminus of BRS3 and a 13-amino
129 acid NanoBiT peptide (HiBiT) to the C-terminus of the G β subunit²⁸. We also employed
130 an engineered G_q protein chimera, similar to the one used in prior structural studies of
131 NMBR and GRPR⁸. Here, 'G_q' refers to this specific engineered chimera. We
132 assembled the BRS3-G_q complexes for cryo-EM by co-expressing and purifying BRS3-
133 LgBiT, G_q, G $\beta\gamma$ -HiBiT, antibody scFv16, and nanobody-35 (Nb35)^{29,30}. These
134 components were processed both in the absence (apo-form) and presence of the
135 ligands BA1 and MK-5046. This approach facilitated the efficient formation and
136 enhanced stability of the apo and ligand-bound BRS3-G_q complexes.

137
138 The single-particle cryo-EM analysis of the collected datasets yielded density maps at
139 nominal global resolutions of 3.5, 2.9, and 3.0 Å for the apo BRS3-G_q-scFv16, BA1-
140 bound BRS3-G_q, and MK-5046-bound BRS3-G_q-scFv16-Nb35 complexes,
141 respectively (Figures 1B-1G, S3-5; Table S2). These maps clearly delineated the
142 positions of the receptor, G-protein trimer, and scFv16/Nb35 in each complex, with
143 most amino acid side chains being resolved (Figure S6). In the apo BRS3-G_q-scFv16
144 complex, the orthosteric binding pocket (OBP) did not exhibit any additional densities.
145 However, for the BA1- and MK-5046-bound complexes, densities for BA1 and MK-
146 5046 were well-resolved, allowing for the construction of atomic models with a high
147 degree of confidence. All three complexes displayed a similar overall structural
148 arrangement, with root mean square deviation (RMSD) values for C_α atoms ranging
149 between 0.3-0.6 Å, indicating minor variations among them (Figures S7A-S7C).

150
151 **Recognition of BA1 by BRS3**
152 In our study, the quality of the cryo-EM maps allowed for the precise modeling of all
153 nine amino acid residues of BA1. This finding aligns with our previous structures of
154 NMB-NMBR and GRP(14-27)-GRPR, where only the C-terminal 9 residues of the
155 longer bombesin agonists (33-residue peptide NMB30 and 14-residue peptide
156 GRP(14-27), respectively) were observed, despite the utilization of the 33-residue
157 peptide NMB30 and the 14-residue peptide GRP(14-27) during complex preparation,
158 respectively (Figures 2A and 2B; Table S3). This suggests that a minimal 9-residue
159 segment might be sufficient for full agonist potency. In the BRS3 structure, BA1 is
160 positioned within the central OBP located in the upper transmembrane domain (TMD),
161 interacting with all extracellular loops and transmembrane segments except TM1. The
162 peptide's C-terminus penetrates deeply into the helical bundle, while the N-terminus of
163 BA1 extends outward towards the extracellular ligand binding cavity. BA1 assumes a
164 dumbbell-shaped conformation, reminiscent of NMB and GRP(14-27) in their
165 respective complexes, underlining a conserved recognition pattern among bombesin

166 receptor family agonists ([Figure 2B](#)). For clarity, all positions of BA1 are numerically
167 designated from the amino terminus of NMB or NMC ([Figure 2A](#)).

168

169 The nine residues of BA1 (residues 2-10) can be categorized into three motifs: the C-
170 terminal HFX(8-10)^{BA1} motif (Where the X is Nle), the middle AV^BA(5-7)^B motif, and the
171 N-terminal ^DFQW(2-4)^{BA1} motif ([Figure 2A](#)). The HFX(8-10)^{BA1} motif adopts an
172 extended structure at the bottom of the OBP, with the side chain of X10^{BA1} penetrating
173 the deepest. The side chains of X10^{BA1} and F9^{BA1} are encased in a hydrophobic cavity
174 comprising L96^{2.53}, L128^{3.33}, V131^{3.36}, C221^{5.42}, F225^{5.46}, W284^{6.48}, A319^{7.42}, and
175 F320^{7.43} ([Figure 2C](#)). These hydrophobic interactions are crucial for BRS3 activation,
176 as demonstrated by significantly reduced potency when L96^{2.53}, L128^{3.33}, and V131^{3.36}
177 are substituted with alanine ([Figures 2F and S8; Table S4](#)). In addition, F9^{BA1} engages
178 in stabilizing π-π packing interactions with the surrounding F225^{5.46}, H288^{6.53} and
179 Y291^{6.55} ([Figure 2D](#)). The H8^{BA1} residue forms hydrogen bonds with S124^{3.29} and
180 S205^{ECL2}, differing from the sandwiching of the corresponding H8 residues in NMB and
181 GRP(14-27) by P^{3.29} and P^{ECL2} in the NMB-NMBR and GRP(14-27)-GRPR structures
182 ([Figures 2D and S7F](#)). The alanine mutations of S124^{3.29} or S205^{ECL2} had a minimal
183 effect on BRS3 activation by BA1, yet, the proline substitution of the S124^{3.29} or
184 S205^{ECL2} substantially lowered the BRS3 activity coordinated by BA1 ([Figures 2D and](#)
185 [S8; Table S4](#)). This highlights the pivotal roles of S124^{3.29} and S205^{ECL2} in peptide BA1
186 recognition by BRS3. H8^B also forms hydrogen bonds with R127^{3.32} and
187 E182^{4.60} ([Figure 2D](#)). Furthermore, the R127^{3.32} also forms a hydrogen bond with the
188 backbone carbonyl of the F9^B, and the R316^{7.39} forms a hydrogen bond with the
189 backbone carbonyl of the H8^B ([Figure 2D](#)). The carboxyl group of the X10^{BA1} forms two
190 hydrogen bonds with the side chains of the R127^{3.32} and R316^{7.39} ([Figure 2D](#)). Mutation
191 of R127^{3.32}, E182^{4.60}, C221^{5.42}, H288^{6.52}, Y291^{6.55} and R316^{7.39} in BRS3 results in a
192 reduced BA1-induced signaling response ([Figures 2F, 2G and S8; Table S4](#)),
193 confirming the essential roles of these residues in BA1 binding and receptor activation.

194

195 The AV^BA(5-7)^{BA1} motif primarily engages in hydrophobic interactions with F191^{ECL2} and
196 F200^{ECL2} from the ECL2, and P304^{ECL3} from ECL3 (Figure 2D). Indeed, alanine
197 mutation of the F200^{ECL2} resulted in decrease in G_q signaling (Figures 2G and S8; Table
198 S4). In addition to the hydrophobic interactions, the backbone carbonyl group of ^BA7^{BA1}
199 formed a hydrogen bond with the backbone amide group of S205^{ECL2}, further stabilizing
200 BA1 binding.

201

202 Following the middle motif, the ^DDFQW(2-4)^{BA1} motif extends along the upper pocket,
203 engaging in π-π interactions with Y108^{2,65}, F200^{ECL2}, H308^{7,31}, and F309^{7,32} from BRS3
204 (Figure 2E). Alanine substitutions at these sites diminish receptor activation compared
205 to the wild-type BRS3 (Figure 2G; Table S4). Anion-π interactions between ^DF2^{BA1} and
206 D193^{ECL2}/D303^{ECL3} also contribute to BA1's binding stability, with alanine mutation of
207 D303^{ECL3} significantly reducing G_q signaling (Figure 2G; Table S4). Furthermore, Q3^{BA1}
208 forms extensive hydrogen bonds with the BRS3 backbone, and its carbonyl group
209 interacts with H107^{2,64} (Figure 2E). In summary, these intricate details reveal the
210 comprehensive mechanism behind BRS3 activation by the synthetic peptide BA1,
211 highlighting the specific interactions and critical residues involved in this process.

212

213 **BRS3 regulation by MK-5046**

214 Continuing our exploration of BRS3, we examined its interaction with MK-5046, the
215 first BRS3-specific nonpeptide receptor agonist (Figure 3). MK-5046 is characterized
216 by distinct functional groups, including a hydroxyl group and a trifluoromethyl group in
217 the central segment, an additional trifluoromethyl group accompanied by a
218 cyclopropane group and an imidazole group on one side, and a benzene ring and a
219 pyrazole group on the other (Figure 3B). The structure of MK-5046-bound BRS3
220 reveals that MK-5046 adopts a "V"-shaped conformation, fitting snugly at the bottom
221 of the BRS3 pocket. Notably, MK-5046, being smaller in volume (475 Å³) than BA1
222 (1089 Å³), occupies a specific sub-pocket that corresponds to the C-terminal HFX(8-
223 10)^{BA1} motif (Figure 3A).

224
225 The trifluoromethyl group, connected to the cyclopropane group, projects towards the
226 upper portion of TM3, establishing extensive fluorine-based halogen bonding
227 interactions with S124^{3.29}, R127^{3.32}, and E182^{4.60} (Figure 3C). Mutations in R127^{3.32} and
228 E182^{4.60} lead to significantly reduced MK-5046-induced signaling (Figures 3E and S8;
229 Table S4), emphasizing the critical roles of these residues in MK-5046 binding and
230 BRS3 activation. Replacement of R127^{3.32} with Q^{3.32} in both NMBR and GRPR
231 receptors notably decreased the E_{max} level for mutated BRS3 (Figures 3E and S8;
232 Table S4), underlining R127^{3.32}'s significance in MK-5046's selectivity for BRS3.

233
234 Additionally, the imidazole, benzene, and pyrazole rings of MK-5046 engage in
235 extensive π-π interactions with W284^{6.48} and Y291^{6.55} of BRS3 (Figure 3C). The
236 interaction between MK-5046's imidazole group and Y291^{6.55} is further reinforced by a
237 hydrogen bond with S205^{ECL2} (Figure 3C). Mutating S205^{ECL2} and Y291^{6.55} results in a
238 considerable decrease in MK-5046-induced BRS3 signaling (Figures 3E and S8; Table
239 S4), confirming their essential role in this interaction. The central hydroxyl group of
240 MK-5046 forms a hydrogen bond with C221^{5.42}, while the central trifluoromethyl group
241 creates robust packing interactions with H288^{6.52}, complemented by π-π packing
242 between W284^{6.48} and H288^{6.52} (Figures 3C and 3D). The opposite side of MK-5046,
243 featuring a benzene ring and pyrazole group, is accommodated within a hydrophobic
244 pocket formed by L96^{2.53}, V131^{3.36}, F225^{5.46}, W284^{6.48}, A319^{7.42}, and F320^{7.43} (Figure
245 3D).

246
247 Previous competitive assays involving MK-5046, Peptide-1 (another pan-BnR agonist),
248 and Bantag-1 (a BRS3-specific peptide antagonist) suggested that MK-5046 functions
249 as an allosteric agonist for BRS3, possibly binding to a distinct pocket from Peptide-
250 1³¹. Our structures show that MK-5046's binding site and pose closely resemble the C-
251 terminal HFX(8-10)^{BA1} motif of BA1 (Figure 3B). The upper trifluoromethyl group of MK-
252 5046 corresponds to the binding site for BA1's H8^B, while its central trifluoromethyl

253 group and benzene ring align with the lower hydrophobic cavity, mirroring the FX(9-
254 10)^B side chains of BA1. The pyrazole group of MK-5046 assumes a position akin to
255 the carboxyl group of BA1's X10^B. In summary, MK-5046's binding pattern shares
256 similarities with the C-terminal HFX(8-10)^{BA1} tripeptide of BA1, suggesting that MK-
257 5046 is an orthosteric agonist. Interestingly, alanine substitution of R316^{7,39} enhances
258 BRS3 activity induced by MK-5046, showing higher efficacy in our IP1 assay ([Figure 3F and S8; Table S4](#)). This finding further underscores the intricate molecular
259 interactions that govern BRS3 regulation and activation by MK-5046.
260

261

262 **Activation of BRS3 by agonists of different types**

263 Understanding how receptor occupation correlates with activation, particularly in the
264 context of peptide and nonpeptide agonists for GPCRs, is crucial. Interestingly, BRS3
265 exhibits a unique behavior in this regard. The binding affinities of the peptide agonist
266 BA1 and the nonpeptide agonist MK-5046 are 2.0 nM and 17 nM^{10,32}, respectively,
267 indicating that BA1 has a nearly 10-fold higher affinity for the receptor than MK-5046.
268 Correspondingly, analysis using dr_sasa reveals that the interface areas for BA1 and
269 MK-5046 are 1094.26 Å² and 429.02 Å², respectively³³. This suggests a direct
270 relationship between a larger buried surface area in the structure and a higher binding
271 affinity.

272

273 However, the activation potency of these agonists presents an intriguing contrast. In
274 our IP1 assays, MK-5046 activates BRS3 with an EC₅₀ value of 0.5 nM, demonstrating
275 26-fold greater potency in activating G_q signaling than BA1, which has an EC₅₀ of 13.0
276 nM. This is notable as most nonpeptide agonists typically exhibit lower potency than
277 the natural peptide agonists of their respective receptors in activating downstream
278 signaling. Yet, MK-5046 surpasses the peptide ligand BA1 in terms of G_q signaling
279 activation.

280

281 To further investigate the potency differences between MK-5046-BRS3 and BA1-BRS3,

282 we conducted molecular dynamics (MD) simulations, each spanning 500 ns over three
283 replicates. These simulations focused on the ligand-binding domain composed of TM3,
284 TM5, and TM6, a region known to influence ligand potency³⁴. The simulations revealed
285 distinct hydrophobic interaction networks in the extracellular TM3-TM5-TM6 region for
286 the two agonists. Specifically, in the MK-5046-BRS3 system, a hydrophobic network
287 surrounding the trifluoromethyl group of MK-5046 was present in 62.9% of the
288 trajectories, compared to only 23.7% in the BA1 system around F9^{BA1}. Representative
289 structures ([Figure 4A](#)) showed that the trifluoromethyl group in MK-5046 engages in
290 electronic interactions with H288^{6.52} and facilitates hydrophobic interactions between
291 F225^{5.46} and V131^{3.36}. In contrast, the larger F9^{BA1} moiety in the BA1 system interacts
292 primarily with V131^{3.36}, disrupting the hydrophobic contact between F225^{5.46} and
293 V131^{3.36} ([Figure 4B](#)).

294

295 Moreover, in the MK-5046 system, the trifluoromethyl group acts as a hydrophobic
296 bridge between H288^{6.52} and F225^{5.46}, stabilizing the activated extracellular TM3-TM5-
297 TM6 conformation. This is evidenced by the fact that direct contact between H288^{6.52}
298 and F225^{5.46} is less frequent (19.9% versus 78.1% in the BA1 system). Consistent with
299 this, the H288A mutation significantly diminishes MK-5046's potency (from 0.53 nM to
300 126.9 nM), while having a less pronounced effect on BA1's binding (from 11.8 nM to
301 68.7 nM) ([Figures 2G, 3F, and 4C](#)). In summary, these findings illustrate the complex
302 and distinct mechanisms by which different types of agonists, both peptide and
303 nonpeptide, activate BRS3. They also highlight the nuanced molecular interactions
304 that govern the receptor's response to these agonists, contributing to our
305 understanding of GPCR activation and signaling.

306

307 **Basis for ligands selectivity of bombesin receptors**

308 In the BnR family, BA1, a synthetic analog, was found to have a high affinity for BRS3,
309 as well as for NMBR and GRPR receptors^{10,35,36} ([Table S1](#)). BRS3 shares
310 approximately 50% amino acid sequence identity with NMBR and 47% with

311 GRPR^{11,37,38}. A closer examination of BA1 binding in BRS3 and GRPR indicates that
312 this synthetic peptide uniquely coordinates with all three bombesin receptors.
313 Structural alignment of the BA1-GRPR-G_q complex (PDB: 7W40)⁹ with our BA1-BRS3-
314 G_q structure showed a high degree of similarity, with an overall C α RMSD of 0.75 Å
315 (**Figure 5A**). Both the ^DFQW(2-4)^B and HFX(8-10)^{BA1} motifs of BA1 align well between
316 BRS3 and GRPR, with notable differences in the side chains of ^DF2^{BA1}, W4^{BA1}, and
317 H8^{BA1} (**Figure 5B**). The key residues in BRS3's upper pocket, including Y108^{2,65},
318 F200^{ECL2}, H308^{7,31}, and F309^{7,32}, involved in π - π interactions with ^DF2^{BA1} and W4^{BA1},
319 are highly conserved in GRPR without substitutions (**Figure 5C**), suggesting a
320 preserved interaction pattern despite conformational differences in these aromatic
321 amino acids. However, in BRS3, the H8^{BA1} side chain deviates from TM3, causing a
322 shift of the middle AV^BA(5-7)^{BA1} motif towards TM6, compared to its position in GRPR
323 (**Figure 5D**). This shift is stabilized by two hydrogen bonds between H8^{BA1} and S124^{3,29}
324 and S205^{45,52} in BRS3. In contrast, BA1's H8 is sandwiched by P^{3,29} and P^{45,52} in GRPR,
325 resembling the coordination seen in NMB-NMBR and GRP(14-27)-GRPR structures
326 (**Figure S7F**). The significant sequence homology and specific flexibility, especially in
327 the ligand-binding pockets, explain BA1's ability to bind all three bombesin receptors.
328

329 The selectivity of natural bombesin-related peptide agonists for individual bombesin-
330 related receptors is an interesting aspect. GRP, the natural ligand for GRPR, has an
331 affinity for GRPR over 650-fold higher than for NMBR and more than 15,000-fold higher
332 than for BRS3. NMB, the natural ligand for NMBR, shows over 650-fold higher affinity
333 for NMBR compared to GRPR and more than 20,000-fold higher than for BRS3 (**Table**
334 **S1**). Prior studies have clarified the determinants of selectivity between NMB30 and
335 GRP(14–27) for NMBR and GRPR^{8,39,40}. In our sequence and structure analyses of
336 these receptors bound with different peptides, we observed five amino acids in the
337 peptide agonist binding pockets that are conserved in both GRPR and NMBR but differ
338 in BRS3: T106^{2,63}, H107^{2,64}, R127^{3,32}, S205^{ECL2}, and H294^{6,58} in BRS3 are substituted
339 by S^{2,63}, R^{2,64}, Q^{3,32}, P^{ECL2}, and R^{6,58}, respectively (**Figure S1**), in NMBR and GRPR. A

340 structure comparison of BA1-BRS3 with NMB-NMBR shows a clash between T6^{NMB} of
341 NMB and S202^{ECL2} of BRS3, which is absent in the equivalent interaction in the BRS3
342 structure due to a shift of BA1's middle motif towards TM6 (Figure 5E). In the BRS3
343 structure, the equivalent V6^{BA1} residue of BA1 shift away from the S202^{ECL2}, due to the
344 shift of the middle AV^BA(5-7)^{BA1} motif towards the TM6. This shift of BA1 middle motif
345 may be a structural characteristic of BRS3 specific ligand, which is favored by the
346 residue combination of the R127^{3.32} and H294^{6.58} substitutions in BRS3 (Figure 5E).
347 Through structural analysis, it is evident that BA1 presents a binding pose of the middle
348 motif nearly identical to the natural agonist GRP in the GRPR structures^{8,9}, located
349 close to TM6 (Figure 5F). Interestingly, the NMB middle motif exhibits a closer
350 alignment with TM2 (Figure 5F). Consequently, these ligand binding poses of NMB and
351 GRP are favored by the conserved residue combination of the Q^{3.32} and R^{6.58}
352 substitutions in NMBR and GRPR receptors. Thus, the Q^{3.32} and R^{6.58} substitutions
353 contribute to the structural characteristics of ligand specific for individual Bn-related
354 receptors, as suggested in the prior mutation studies⁴¹. For NMB, it has been reported
355 that T6^{NMB} forms a hydrogen bond with the main carboxyl group of L3^{NMB}, playing a
356 pivotal role in NMB binding and selectivity by NMBR^{8,9}. The clash of the T6^{NMB} here
357 possibly contributes to the weak binding of the NMB by BRS3.

358

359 In addition, structure comparison of the BA1-BRS3 with our previously reported
360 GRP(14-27)-GRPR structure (PDB code: 8H0Q) reveals that the T106^{2.63} substitution
361 in BRS3 induces an inward push of the side chain of W113^{ECL1} (Figure 5G). This
362 movement is further stabilized by the packing between the side chain of W113^{ECL1} and
363 the H107^{2.64} substitution in BRS3, along with the conserved disulfide bond formed by
364 C120^{3.25} and C203^{ECL2} (Figure 5G). Together with the main chain carboxyl group of
365 E201^{ECL2}, the inward shift of W113^{ECL1} subsequently results in an inward movement of
366 the EGW(111-113)^{ECL1} of BRS3, causing a clash with the crucial residue H3^{GRP} of
367 GPR(14-27) (Figure 5H). When we compare the BA1-BRS3 with the other GRP-GRPR
368 structure (PDB code: 7W3Z), a clash between the H3^{GRP} and the carboxyl group of

369 E201^{ECL2} can also be observed (**Figure S7G**), despite the H3^{GRP} here adopt a rotamer
370 conformation due to the similar ECL1 positions between the BRS3 and GRPR
371 structures. Interestingly, the H3^{GRP} was also reported to accommodate the featured
372 ECL2 of GRPR, and contribute to the weak binding of GRP to NMBR^{8,39}, suggesting
373 its pivotal role of selectivity for GPR(14-27) in BnR family. Overall, these structural
374 insights highlight the unique features of BRS3 that contribute to its low affinity for
375 bombesin-related natural ligands like NMB and GRP.

376

377 **Common activation features of bombesin receptors subfamily**

378 In examining the significant structural similarities between the BA1- and MK-5046-
379 bound BRS3 complexes, we chose the BA1-BRS3 complex for a detailed analysis of
380 BRS3 activation. Comparing the active BA1-bound BRS3-G_q complex with both the
381 active structure of GRPR bound to BA1 (PDB: 7W40) and the inactive structure of
382 GRPR bound to a synthetic antagonist, PD176252 (PDB: 7W41), we observe that
383 BRS3 exhibits classic activation features typical of Class A GPCRs in response to BA1.
384 Notably, the cytoplasmic end of TM6 in BRS3 displays a pronounced outward
385 movement while the cytoplasmic part of TM7 shifts inward. This rearrangement
386 accommodates the C-terminal α 5 helix of the G α _q subunit, a key feature of Class A
387 GPCR activation (**Figures 6A-6C**). Additionally, the extracellular end of TM1 in the BA1-
388 bound BRS3 shifts 5.3 Å towards TM7, similar to movements observed in NMBR and
389 GRPR structures (**Figures 6B and S7H**).

390

391 In comparison to PD176252, BA1 binds deeper within the orthosteric pocket,
392 surrounded by TM3, TM6, and TM7, and forms hydrophobic contacts with W284^{6,48}
393 (**Figure 6D**). BA1's binding causes a significant deflection of the W284^{6,48} indole ring,
394 initiating a cascade of conformational changes linked to receptor activation⁴² (**Figure**
395 **6D**). This process mirrors the classic activation mechanism seen in Class A GPCRs,
396 where the displacement of W284^{6,48} exerts a downward force on F280^{6,44} in the
397 conserved P^{5.50}V^{3.40}F^{6,44} core triad, leading to changes in the D^{3.49}R^{3.50}Y^{3.51} motif

398 (Figures 6D-6F). Additionally, the conserved N^{7.49}P^{7.50}xxY^{7.53} motif is replaced with a
399 N^{7.49}P^{7.50}xxL^{7.53} motif in BRS3. In the structure, BA1's X10^{BA1} carboxyl group forms a
400 hydrogen bond with R316^{7.39}, contributing to activating the N^{7.49}P^{7.50}xxL^{7.53} motif in
401 BRS3. Typically, the conserved Y^{7.53} in this motif undergoes a significant rotation
402 towards TM3, leading to TM7's inward movement⁴³. However, in BRS3, the leucine
403 substitution at Y^{7.53} undergoes a lateral shift towards TM1 and TM2, highlighting a
404 unique yet conserved activation mechanism shared among bombesin receptors.

405
406 During BRS3 activation, the P^{5.50}V^{3.40}F^{6.44} and N^{7.49}P^{7.50}xxL^{7.53} motifs, which link the
407 ligand-binding pocket to the G protein-coupling interface, undergo rearrangements.
408 These involve movements of F^{6.44} and L^{7.53}, triggering significant outward shifts of TM5
409 and TM6 (3.4 Å at R^{5.63}; 8.1 Å at R^{6.30}), thereby facilitating the engagement of the G_{αq}
410 subunit's C-terminus. This feature is consistent with activation mechanisms observed
411 across GPCRs (Figure 6C; Table S5). These structural insights from our BRS3 studies
412 enhance our understanding of the activation mechanisms within the bombesin receptor
413 subfamily, demonstrating how specific molecular changes lead to receptor activation.

414

415 Comparison with the AlphaFold2-predicted structure

416 We compared our cryo-EM resolved structures with the structure predicted by
417 AlphaFold2, specifically focusing on the receptor domain (Figure S7I). Given the
418 notable structural similarities between the BA1- and MK-5046-bound BRS3 complexes,
419 we selected the BA1-BRS3 complex for further analysis. The resolved BA1-BRS3
420 structure and the AlphaFold2-predicted structure exhibited somewhat dissimilar overall
421 arrangements, with a C_α RMSD of 1.5 Å. Despite AlphaFold2 capturing the general
422 backbone contours of the receptor, substantial discrepancies existed between the
423 predicted models and experimental structures regarding the assembly of the
424 extracellular and transmembrane domains. Compared to the BA1-BRS3 structure, the
425 AlphaFold2 structure represents an inactive conformation, with the intracellular part of
426 TM5 tilting outward and the intracellular part of TM6 shifting inward. Specifically, the

427 key residues in the OBP in the AlphaFold2 BRS3 structure, including H107^{2,64}, S124^{3,29},
428 R127^{3,32}, W284^{6,48} ([Figure S7J](#)), adopt distinct positions that cannot further favor the
429 BA1 binding. In conclusion, while the AlphaFold2-predicted model serves as a valuable
430 reference point, obtaining additional empirical structural information is imperative to
431 accurately guide drug design.

432

433 **Discussion**

434 Our study on BRS3, an orphan member of the bombesin receptor subfamily, offers
435 significant insights into the complex dynamics and mechanisms of GPCRs. As orphan
436 receptors, entities like BRS3, without identified endogenous ligands, present
437 challenges in understanding their roles, particularly in physiological and pathological
438 contexts like metabolic diseases and cancer⁴⁴⁻⁴⁶.

439

440 The structural analysis of BRS3 in its apo form and when bound to the synthetic analog
441 BA1 and the nonpeptide agonist MK-5046 reveals a high degree of structural
442 conservation ([Figure S7A](#)). This similarity, despite the evolutionary loss of binding to
443 natural ligands like NMB and GRP in placental mammals, underscores the evolutionary
444 adaptability of BRS3⁴⁷. Unlike other orphan receptors that drive constitutive activation
445 through their ECL2s, such as GPR12 and GPR21⁴⁸⁻⁵⁰, BRS3 does not exhibit this
446 feature, indicating unique structural and functional characteristics.

447

448 Our investigation reveals unique aspects of ligand recognition and activation in BRS3.
449 The complex interplay of residues within the receptor's binding site, including those
450 contributing to agonist-induced activation, highlights the receptor's intricate regulation
451 mechanisms. These findings provide a foundation for the future exploration of BRS3
452 as a potential therapeutic target, particularly in diseases linked to dysfunctional GPCR
453 signaling.

454

455 In the bombesin receptor family, the synthetic analog BA1 exhibits high affinity for
456 BRS3, NMBR and GRPR. Our structural analysis comparing the BA1 complexes with

457 BRS3 and GRPR shows that the overall binding mode of BA1 to the two receptors is
458 highly similar despite some differences in their amino acid side chains. This is largely
459 attributable to the high homology of key residues in the ligand binding pockets of these
460 receptors. These findings explain BA1's ability to bind all members of the BnR family.
461 On the other hand, natural peptides like NMB and GRP demonstrate high selectivity
462 for individual BnR receptors. Our sequence and structural comparisons of apo and
463 peptide-bound BRS3 identified five key residues that differ from NMBR and GRPR,
464 which may account for its low affinity for NMB and GRP. This provides evidence to
465 understand the loss of binding to these natural peptides by BRS3. Our study offers
466 insights into the structural basis of ligand selectivity, aiding efforts to design BRS3
467 peptide ligands with high selectivity.

468

469 In addition to these findings, our research aligns with the classical activation features
470 observed in Class A GPCRs, including the outward movement of TM6 and the inward
471 shift of TM7 in response to BA1 binding. This conformational change, particularly the
472 deflection of the W284^{6,48} indole ring, echoes activation mechanisms seen in other
473 GPCRs. Such structural insights into BRS3, in tandem with its evolutionary trajectory,
474 contribute to a deeper understanding of its functions and potential therapeutic
475 implications.

476

477 Our comprehensive study, therefore, not only unravels the unique structural and
478 functional attributes of BRS3 but also enhances the overall understanding of GPCR
479 activation mechanisms. This knowledge is crucial for developing targeted interventions
480 for diseases associated with GPCR dysfunction. Future research is needed to delve
481 deeper into BRS3's self-activation mechanism and explore its potential as a
482 therapeutic target within the bombesin receptor family.

483

484 **Competing interests**

485 The authors declare no competing interests.

486

487 **Data Resources**

488 Materials are available from the corresponding authors upon reasonable request.
489 Density maps and structure coordinates have been deposited in the Electron
490 Microscopy Data Bank (EMDB) and the Protein Data Bank (PDB) with accession codes
491 EMD-38927 and 8Y51 for apo BRS3-G_q-scFv16 complex; EMD-38928 and 8Y52 for
492 BA1-bound BRS3-G_q complex; and EMD-38929 and 8Y53 for MK-5046-bound BRS3-
493 G_q complex. Source data are provided with this paper.

494

495 **Reference**

- 496 1. Flock, T., Hauser, A.S., Lund, N., Gloriam, D.E., Balaji, S., and Babu, M.M. (2017). Selectivity
497 determinants of GPCR-G-protein binding. *Nature* *545*, 317-322. 10.1038/nature22070.
- 498 2. Probst, W.C., Snyder, L.A., Schuster, D.I., Brosius, J., and Sealfon, S.C. (1992). Sequence
499 Alignment of the G-Protein Coupled Receptor Superfamily. *DNA and Cell Biology* *11*, 1-
500 20. DOI 10.1089/dna.1992.11.1.
- 501 3. Jensen, R.T., Battey, J.F., Spindel, E.R., and Benya, R.V. (2008). International union of
502 pharmacology. LXVIII. Mammalian bombesin receptors: Nomenclature, distribution,
503 pharmacology, signaling, and functions in normal and disease states. *Pharmacol Rev* *60*,
504 1-42. 10.1124/pr.107.07108.
- 505 4. Ladenheim, E.E., Behles, R.R., Bi, S., and Moran, T.H. (2009). Gastrin-Releasing Peptide
506 Messenger Ribonucleic Acid Expression in the Hypothalamic Paraventricular Nucleus Is
507 Altered by Melanocortin Receptor Stimulation and Food Deprivation. *Endocrinology* *150*,
508 672-678. 10.1210/en.2008-0559.
- 509 5. Karatsoreos, I.N., Romeo, R.D., McEwen, B.S., and Silver, R. (2006). Diurnal regulation of
510 the gastrin-releasing peptide receptor in the mouse circadian clock. *Eur J Neurosci* *23*,
511 1047-1053. 10.1111/j.1460-9568.2006.04633.x.
- 512 6. Sun, Y.G., and Chen, Z.F. (2007). A gastrin-releasing peptide receptor mediates the itch
513 sensation in the spinal cord. *Nature* *448*, 700-703. 10.1038/nature06029.
- 514 7. Sun, Y.G., Zhao, Z.Q., Meng, X.L., Yin, J., Liu, X.Y., and Chen, Z.F. (2009). Cellular Basis of
515 Itch Sensation. *Science* *325*, 1531-1534. 10.1126/science.1174868.
- 516 8. Li, C.Y., Xu, Y.W., Liu, H., Cai, H.M., Jiang, Y., Xu, H.E., and Yin, W.C. (2023). Molecular
517 recognition of itch-associated neuropeptides by bombesin receptors. *Cell Res* *33*, 184-
518 187. 10.1038/s41422-022-00743-6.
- 519 9. Peng, S.M., Zhan, Y.T., Zhang, D.Q., Ren, L., Chen, A.Q., Chen, Z.F., and Zhang, H.T. (2023).
520 Structures of human gastrin-releasing peptide receptors bound to antagonist and agonist
521 for cancer and itch therapy. *P Natl Acad Sci USA* *120*. ARTN
522 e221623012010.1073/pnas.2216230120.
- 523 10. Mantey, S.A., Weber, H.C., Sainz, E., Akeson, M., Ryan, R.R., Pradhan, T.K., Searles, R.P.,
524 Spindel, E.R., Battey, J.F., Coy, D.H., and Jensen, R.T. (1997). Discovery of a high affinity
525 radioligand for the human orphan receptor, bombesin receptor subtype 3, which

- 526 demonstrates that it has a unique pharmacology compared with other mammalian
527 bombesin receptors. *Journal of Biological Chemistry* **272**, 26062-26071. DOI
528 10.1074/jbc.272.41.26062.
- 529 11. Fathi, Z., Corjay, M.H., Shapira, H., Wada, E., Benya, R., Jensen, R., Viallet, J., Sausville, E.A.,
530 and Battey, J.F. (1993). Brs-3 - A Novel Bombesin Receptor Subtype Selectively Expressed
531 in Testis and Lung-Carcinoma Cells. *Journal of Biological Chemistry* **268**, 5979-5984.
- 532 12. Uehara, H., Hocart, S.J., González, N., Mantey, S.A., Nakagawa, T., Katsuno, T., Coy, D.H.,
533 and Jensen, R.T. (2012). The molecular basis for high affinity of a universal ligand for
534 human bombesin receptor (BnR) family members. *Biochemical Pharmacology* **84**, 936-
535 948. 10.1016/j.bcp.2012.07.010.
- 536 13. Moreno-Villegas, Z., Martín-Duce, A., Aparicio, C., Portal-Núñez, S., Sanz, R., Mantey, S.A.,
537 Jensen, R.T., Lorenzo, O., Egido, J., and González, N. (2018). Activation of bombesin
538 receptor Subtype-3 by [D-Tyr, β -Ala,Phe,Nle]bombesin increased glucose uptake and
539 lipogenesis in human and rat adipocytes. *Mol Cell Endocrinol* **474**, 10-19.
540 10.1016/j.mce.2018.01.028.
- 541 14. Sebhat, I.K., Franklin, C., Lo, M.M.C., Chen, D., Jewell, J.P., Miller, R., Pang, J.M., Palyha, O.,
542 Kan, Y.Q., Kelly, T.M., et al. (2011). Discovery of MK-5046, a Potent, Selective Bombesin
543 Receptor Subtype-3 Agonist for the Treatment of Obesity. *Acs Medicinal Chemistry
Letters* **2**, 43-47. 10.1021/ml100196d.
- 544 15. Reitman, M.L., Dishy, V., Moreau, A., Denney, W.S., Liu, C.C., Kraft, W.K., Mejia, A.V., Matson,
545 M.A., Stoch, S.A., Wagner, J.A., and Lai, E. (2012). Pharmacokinetics and
546 Pharmacodynamics of MK-5046, a Bombesin Receptor Subtype-3 (BRS-3) Agonist, in
547 Healthy Patients. *Journal of Clinical Pharmacology* **52**, 1306-1316.
548 10.1177/0091270011419854.
- 549 16. Wu, L.H., Cui, J.H., Zhao, C.X., Wang, Z.Y., Lu, J.H., Li, S.S., Jia, J.P., Xiao, H., and Zhang, Y.
550 (2023). Discovery of Dimethyl Shikonin Oxime 5a, a Potent, Selective Bombesin Receptor
551 Subtype-3 Agonist for the Treatment of Type 2 Diabetes Mellitus. *Journal of Medicinal
Chemistry*. 10.1021/acs.jmedchem.3c00323.
- 552 17. Zhu, Y.A., Wu, L.H., Zhao, Y.X., Wang, Z.Y., Lu, J.H., Yu, Y., Xiao, H., and Zhang, Y. (2022).
553 Discovery of oridonin as a novel agonist for BRS-3. *Phytomedicine* **100**. ARTN
554 15408510.1016/j.phymed.2022.154085.
- 555 18. Wu, L., Cui, J., Zhao, C., Wang, Z., Lu, J., Li, S., Jia, J., Xiao, H., and Zhang, Y. (2023). Discovery
556 of Dimethyl Shikonin Oxime 5a, a Potent, Selective Bombesin Receptor Subtype-3 Agonist
557 for the Treatment of Type 2 Diabetes Mellitus. *J Med Chem* **66**, 8011-8029.
558 10.1021/acs.jmedchem.3c00323.
- 559 19. He, H.B., Jiang, H., Chen, Y., Ye, J., Wang, A.L., Wang, C., Liu, Q.S., Liang, G.L., Deng, X.M.,
560 Jiang, W., and Zhou, R.B. (2018). Oridonin is a covalent NLRP3 inhibitor with strong anti-
561 inflammasome activity. *Nature Communications* **9**. ARTN 255010.1038/s41467-018-
562 04947-6.
- 563 20. Bu, H., Liu, D., Zhang, G., Chen, L., and Song, Z. (2020). AMPK/mTOR/ULK1 Axis-Mediated
564 Pathway Participates in Apoptosis and Autophagy Induction by Oridonin in Colon Cancer
565 DLD-1 Cells. *Onco Targets Ther* **13**, 8533-8545. 10.2147/OTT.S262022.
- 566 21. OhkiHamazaki, H., Watase, K., Yamamoto, K., Ogura, H., Yamano, M., Yamada, K., Maeno,
567 H., Imaki, J., Kikuyama, S., Wada, E., and Wada, K. (1997). Mice lacking bombesin receptor

- 570 subtype-3 develop metabolic defects and obesity. *Nature* *390*, 165-169. DOI
571 10.1038/36568.
- 572 22. Yamada, K., Santo-Yamada, Y., Wada, E., and Wada, K. (2002). Role of bombesin (BN)-like
573 peptides/receptors in emotional behavior by comparison of three strains of BN-like
574 peptide receptor knockout mice. *Mol Psychiatr* *7*, 113-117. DOI 10.1038/sj/mp/4000974.
- 575 23. Ladenheim, E.E., Hamilton, N.L., Behles, R.R., Bi, S., Hampton, L.L., Battey, J.F., and Moran,
576 T.H. (2008). Factors contributing to obesity in bombesin receptor subtype -3-deficient
577 mice. *Endocrinology* *149*, 971-978. 10.1210/en.2007-1319.
- 578 24. Guan, X.M., Chen, H., Dobbelaar, P.H., Dong, Y., Fong, T.M., Gagen, K., Gorski, J., He, S.W.,
579 Howard, A.D., Jian, T.Y., et al. (2010). Regulation of Energy Homeostasis by Bombesin
580 Receptor Subtype-3: Selective Receptor Agonists for the Treatment of Obesity. *Cell
581 Metabolism* *11*, 101-112. 10.1016/j.cmet.2009.12.008.
- 582 25. Pinol, R.A., Zahler, S.H., Li, C., Saha, A., Tan, B.K., Skop, V., Gavrilova, O., Xiao, C., Krashes,
583 M.J., and Reitman, M.L. (2018). Brs3 neurons in the mouse dorsomedial hypothalamus
584 regulate body temperature, energy expenditure, and heart rate, but not food intake. *Nat
585 Neurosci* *21*, 1530-1540. 10.1038/s41593-018-0249-3.
- 586 26. Nakamichi, Y., Wada, E., Aoki, K., Ohara-Imaizumi, M., Kikuta, T., Nishiwaki, C., Matsushima,
587 S., Watanabe, T., Wada, K., and Nagamatsu, S. (2004). Functions of pancreatic β cells and
588 adipocytes in bombesin receptor subtype -3-deficient mice. *Biochem Bioph Res Co* *318*,
589 698-703. 10.1016/j.bbrc.2004.04.081.
- 590 27. Chun, E., Thompson, A.A., Liu, W., Roth, C.B., Griffith, M.T., Katritch, V., Kunken, J., Xu, F.,
591 Cherezov, V., Hanson, M.A., and Stevens, R.C. (2012). Fusion partner toolchest for the
592 stabilization and crystallization of G protein-coupled receptors. *Structure* *20*, 967-976.
593 10.1016/j.str.2012.04.010.
- 594 28. Duan, J., Shen, D.D., Zhou, X.E., Bi, P., Liu, Q.F., Tan, Y.X., Zhuang, Y.W., Zhang, H.B., Xu,
595 P.Y., Huang, S.J., et al. (2020). Cryo-EM structure of an activated VIP1 receptor-G protein
596 complex revealed by a NanoBiT tethering strategy. *Nature Communications* *11*. ARTN
597 412110.1038/s41467-020-17933-8.
- 598 29. Rasmussen, S.G.F., DeVree, B.T., Zou, Y.Z., Kruse, A.C., Chung, K.Y., Kobilka, T.S., Thian, F.S.,
599 Chae, P.S., Pardon, E., Calinski, D., et al. (2011). Crystal structure of the β adrenergic
600 receptor-Gs protein complex. *Nature* *477*, 549-U311. 10.1038/nature10361.
- 601 30. Maeda, S., Koehl, A., Matile, H., Hu, H.L., Hilger, D., Schertler, G.F.X., Manglik, A., Skiniotis,
602 G., Dawson, R.J.P., and Kobilka, B.K. (2018). Development of an antibody fragment that
603 stabilizes GPCR/G-protein complexes. *Nature Communications* *9*. ARTN
604 371210.1038/s41467-018-06002-w.
- 605 31. Ramos-Alvarez, I., Iordanskaia, T., Mantey, S.A., and Jensen, R.T. (2022). The Nonpeptide
606 Agonist MK-5046 Functions As an Allosteric Agonist for the Bombesin Receptor Subtype -
607 3. *Journal of Pharmacology and Experimental Therapeutics* *382*, 66-78.
608 10.1124/jpet.121.001033.
- 609 32. Moreno, P., Mantey, S.A., Nuche-Berenguer, B., Reitman, M.L., González, N., Coy, D.H.,
610 and Jensen, R.T. (2013). Comparative Pharmacology of Bombesin Receptor Subtype-3,
611 Nonpeptide Agonist MK-5046, a Universal Peptide Agonist, and Peptide Antagonist
612 Bantag-1 for Human Bombesin Receptors. *Journal of Pharmacology and Experimental
613 Therapeutics* *347*, 100-116. 10.1124/jpet.113.206896.

- 614 33. Ribeiro, J., Ríos-Vera, C., Melo, F., and Schüller, A. (2019). Calculation of accurate
615 interatomic contact surface areas for the quantitative analysis of non-bonded molecular
616 interactions. *Bioinformatics* *35*, 3499-3501. 10.1093/bioinformatics/btz062.
- 617 34. Heydenreich, F.M., Marti-Solano, M., Sandhu, M., Kobilka, B.K., Bouvier, M., and Babu, M.M.
618 Molecular determinants of ligand efficacy and potency in GPCR signaling. *Science* *382*,
619 eadh1859. 10.1126/science.adh1859.
- 620 35. Uehara, H., González, N., Sancho, V., Mantey, S.A., Nuche-Berenguer, B., Pradhan, T., Coy,
621 D.H., and Jensen, R.T. (2011). Pharmacology and selectivity of various natural and synthetic
622 bombesin related peptide agonists for human and rat bombesin receptors differs.
623 *Peptides* *32*, 1685-1699. 10.1016/j.peptides.2011.06.017.
- 624 36. Hoppenz, P., Els-Heindl, S., and Beck-Sickinger, A.G. (2019). Identification and stabilization
625 of a highly selective gastrin-releasing peptide receptor agonist. *Journal of Peptide Science*
626 *25*. ARTN e322410.1002/psc.3224.
- 627 37. Gorbulev, V., Akhundova, A., Buchner, H., and Fahrenholz, F. (1992). Molecular-Cloning
628 of a New Bombesin Receptor Subtype Expressed in Uterus during Pregnancy. *European
629 Journal of Biochemistry* *208*, 405-410. DOI 10.1111/j.1432-1033.1992.tb17201.x.
- 630 38. OhkiHamazaki, H., Wada, E., Matsui, K., and Wada, K. (1997). Cloning and expression of
631 the neuromedin B receptor and the third subtype of bombesin receptor genes in the
632 mouse. *Brain Research* *762*, 165-172. Doi 10.1016/S0006-8993(97)00380-6.
- 633 39. Lin, J.T., Coy, D.H., Mantey, S.A., and Jensen, R.T. (1995). Comparison of the peptide
634 structural requirements for high affinity interaction with bombesin receptors. *European
635 Journal of Pharmacology* *294*, 55-69. Doi 10.1016/0014-2999(95)00510-2.
- 636 40. Tokita, K., Hocart, S.J., Coy, D.H., and Jensen, R.T. (2002). Molecular basis of the selectivity
637 of gastrin-releasing peptide receptor for gastrin-releasing peptide. *Mol Pharmacol* *61*,
638 1435-1443. UNSP 1472/985354DOI 10.1124/mol.61.6.1435.
- 639 41. Gonzalez, N., Hocart, S.J., Portal-Nuñez, S., Mantey, S.A., Nakagawa, T., Zudaire, E., Coy,
640 D.H., and Jensen, R.T. (2008). Molecular basis for agonist selectivity and activation of the
641 orphan bombesin receptor subtype 3 receptor. *Journal of Pharmacology and
642 Experimental Therapeutics* *324*, 463-474. 10.1124/jpet.107.132332.
- 643 42. Weis, W.I., and Kobilka, B.K. (2018). The Molecular Basis of G Protein-Coupled Receptor
644 Activation. *Annual Review of Biochemistry*, Vol *87* *87*, 897-919. 10.1146/annurev-
645 biochem-060614-033910.
- 646 43. Zhou, Q.T., Yang, D.H., Wu, M., Guo, Y., Guo, W.J., Zhong, L., Cai, X.Q., Dai, A.T., Jang, W.J.,
647 Shakhnovich, E.I., et al. (2019). Common activation mechanism of class A GPCRs. *eLife* *8*.
648 ARTN e5027910.7554/eLife.50279.
- 649 44. Foster, S.R., Hauser, A.S., Vedel, L., Strachan, R.T., Huang, X.P., Gavin, A.C., Shah, S.D.,
650 Nayak, A.P., Haugaard-Kedstrom, L.M., Penn, R.B., et al. (2019). Discovery of Human
651 Signaling Systems: Pairing Peptides to G Protein-Coupled Receptors. *Cell* *179*, 895-
652 908.e821. 10.1016/j.cell.2019.10.010.
- 653 45. Pérez-Gómez, E., Andrades, C., Flores, J.M., Quintanilla, M., Paramio, J.M., Guzmán, M.,
654 and Sánchez, C. (2013). The orphan receptor GPR55 drives skin carcinogenesis and is
655 upregulated in human squamous cell carcinomas. *Oncogene* *32*, 2534-2542.
656 10.1038/onc.2012.278.
- 657 46. Marsango, S., Barki, N., Jenkins, L., Tobin, A.B., and Milligan, G. (2022). Therapeutic

- 658 validation of an orphan G protein-coupled receptor: The case of GPR84. *Brit J Pharmacol*
659 *179*, 3529-3541. 10.1111/bph.15248.
- 660 47. Tang, H.H., Shu, C.J., Chen, H.D., Zhang, X.J., Zang, Z.Q., and Deng, C. (2019). Constitutively
661 active BRS3 is a genuinely orphan GPCR in placental mammals. *Plos Biology* *17*. ARTN
662 e300017510.1371/journal.pbio.3000175.
- 663 48. Lin, X., Chen, B., Wu, Y.R., Han, Y.Q., Qi, A., Wang, J.Y., Yang, Z., Wei, X.H., Zhao, T.T., Wu,
664 L.J., et al. (2023). Cryo-EM structures of orphan GPR21 signaling complexes. *Nature
Communications* *14*. ARTN 21610.1038/s41467-023-35882-w.
- 666 49. Li, H., Zhang, J.Y., Yu, Y.A., Luo, F., Wu, L.J., Liu, J.L., Chen, N., Liu, Z.J., and Hua, T. (2023).
667 Structural insight into the constitutive activity of human orphan receptor GPR12. *Sci Bull*
668 *68*, 95-104. 10.1016/j.scib.2022.12.023.
- 669 50. Lin, X., Li, M.Y., Wang, N.D., Wu, Y.R., Luo, Z.P., Guo, S.M., Han, G.W., Li, S.B., Yue, Y., Wei,
670 X.H., et al. (2020). Structural basis of ligand recognition and self-activation of orphan
671 GPR52. *Nature* *579*, 152-+. 10.1038/s41586-020-2019-0.

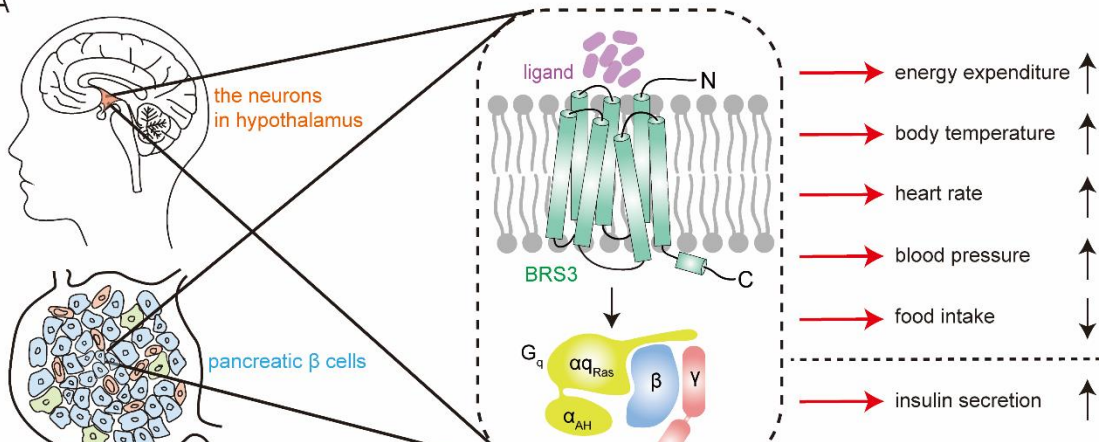
672

673

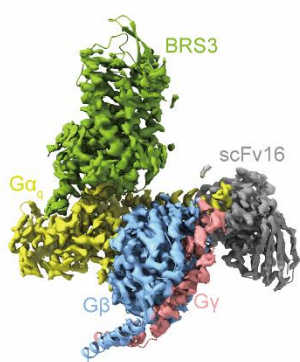
674 **FIGURES**

Figure 1

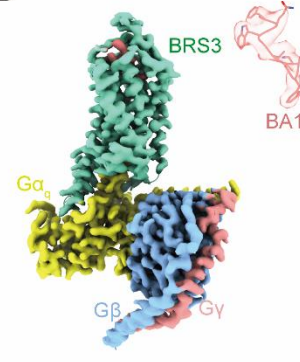
A



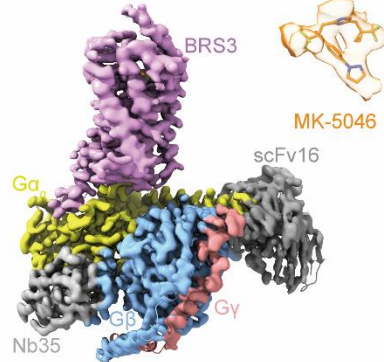
B



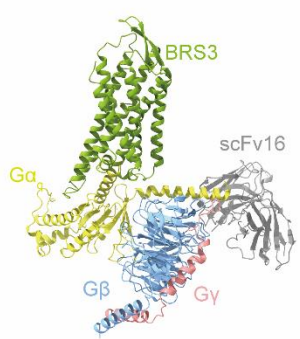
D



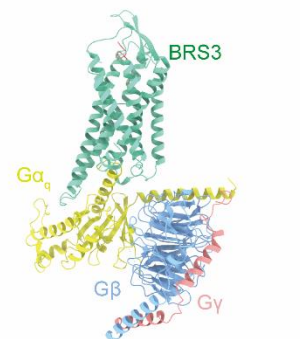
F



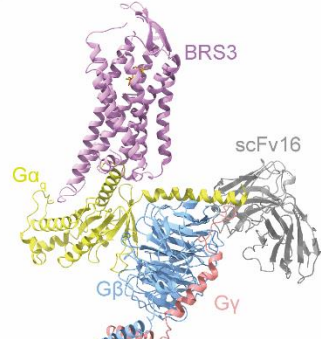
C



E



G



675

676 **Figure 1. Cryo-EM structures of BRS3-G_q complexes, both in the absence (apo-
677 form) and presence of the ligands BA1 and MK-5046.**

678 (A) Schematic illustration of the BRS3 function in the regulation of metabolism
679 pathways. Briefly, activation of BRS3 neurons in the hypothalamus increased
680 sympathetic nervous tone, elevating energy expenditure, body temperature, heart
681 rate, and blood pressure via brown adipose tissue, heart, and arteries, respectively.
682 And agonists activate BRS3 on pancreatic β cells, leading to an increase in glucose-

683 stimulated insulin secretion.

684 (B and C) Orthogonal views of the density map (B) and model (C) for the apo BRS3-

685 G_q complex. The receptor BRS3 is displayed in forest green. The heterotrimeric G_q

686 proteins are colored by subunits: Gα_q, yellow; Gβ, cornflower blue; Gγ, deep salmon;

687 scFv16, gray.

688 (D and E) Orthogonal views of the density map (D) and model (E) of the BA1-BRS3-

689 G_q complex. BA1 is shown in light salmon; the receptor BRS3 is displayed in

690 aquamarine. The heterotrimeric G_q proteins are colored by subunits: Gα_q, yellow; Gβ,

691 cornflower blue; Gγ, deep salmon.

692 (F and G) Orthogonal views of the density map (F) and model (G) of the MK-5046-

693 BRS3-G_q complex. MK-5046 is shown in orange; the receptor BRS3 is displayed in

694 violet. The heterotrimeric G_q proteins are colored by subunits: Gα_q, yellow; Gβ,

695 cornflower blue; Gγ, deep salmon; scFv16, gray.

696

697

698

699

700

701

702

703

704

705

706

707

708

709

710

711

712

713

714

715

716

717

718

719

720

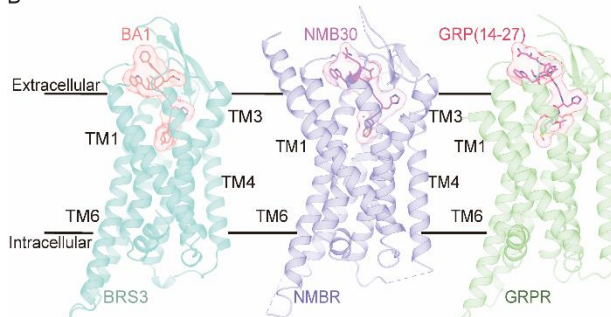
Figure 2

A

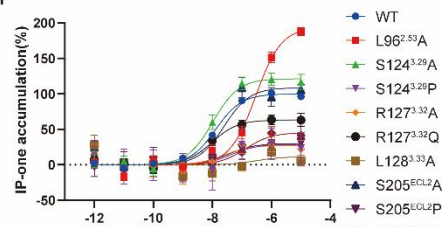
BA1	2	3	4	5	6	7	8	9	10
	^D Phe	Gln	Trp	Ala	Val	^B Ala	His	Phe	Nle
NMB	Gly	Asn	Leu	Trp	Ala	Thr	Gly	His	Phe
NMC	Gly	Asn	His	Trp	Ala	Val	Gly	His	Leu

Met-NH₂

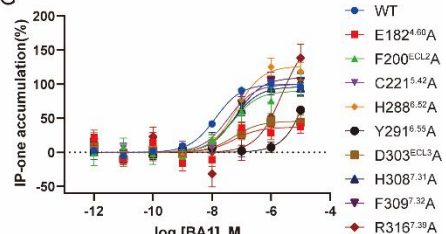
B



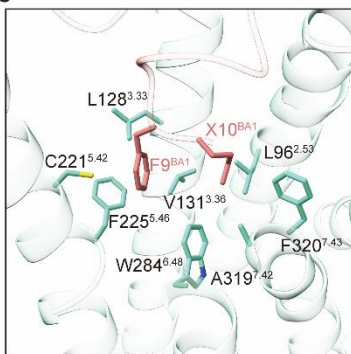
F



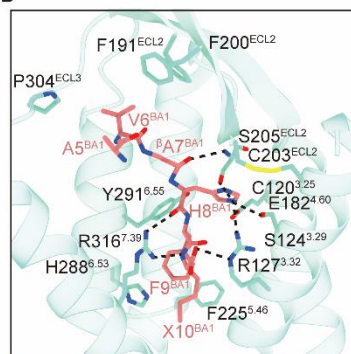
G



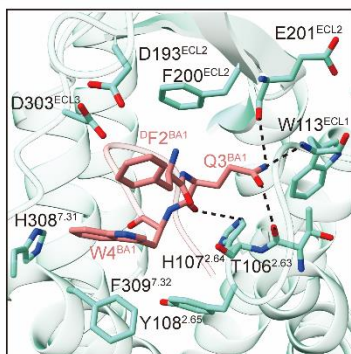
C



D



E



721

722 Figure 2. The BA1-binding pocket in BRS3.

723 (A) The sequence of BA1 peptide. The amino acid numbering of BA1 is determined
724 relative to NMB. See also Table S3.

725 (B) Side views of the ligands-binding pocket in bombesin receptors family.

726 (C-E) Detailed interactions of BA1 with BRS3. Hydrogen bonds are depicted as black
727 dashed lines.

728 (F and G) Effects of mutations in the BA1-binding pocket in IP1 assay. Data are
729 presented as mean \pm S.E.M. of at least three independent experiments. Source
730 data are available online.

731

732

733

734

735

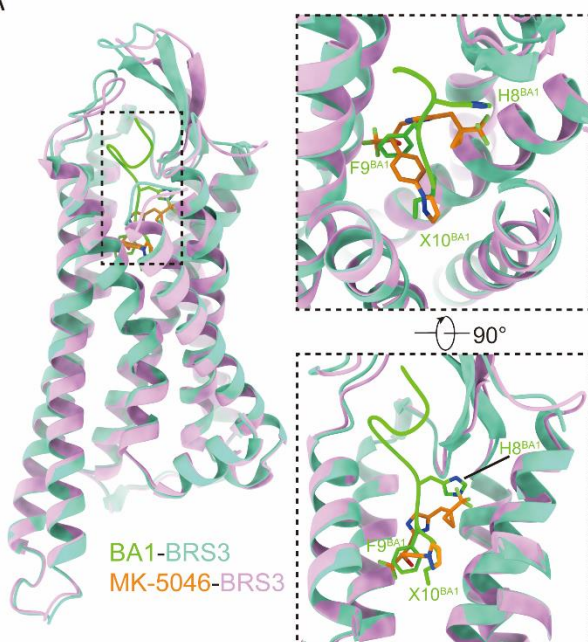
736

737

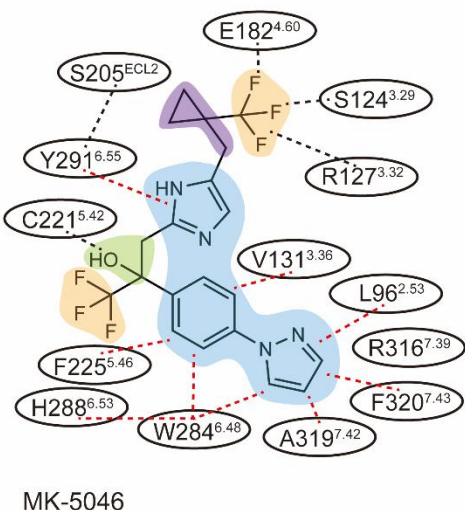
738

Figure 3

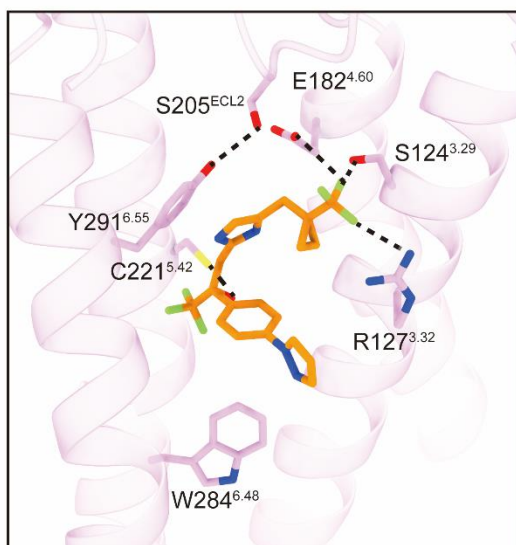
A



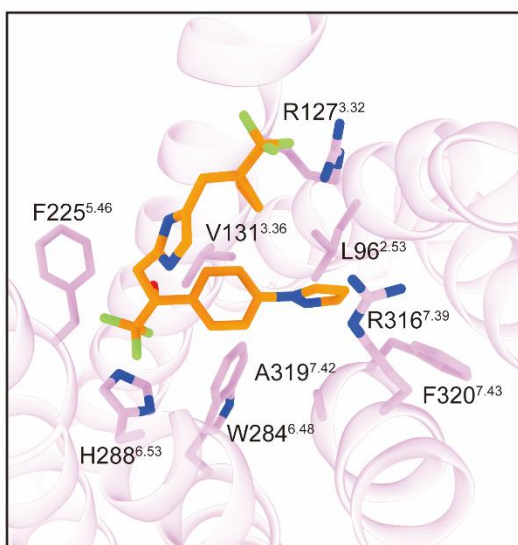
B



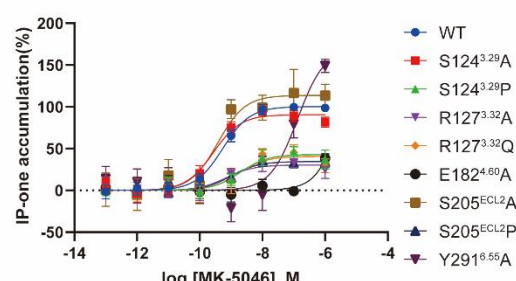
C



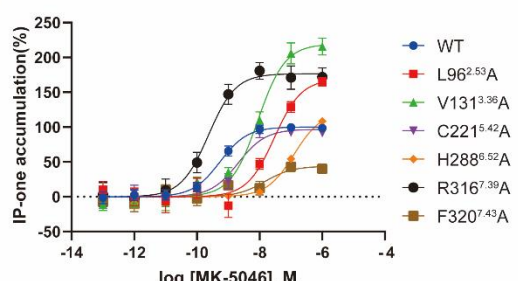
D



E



F



739

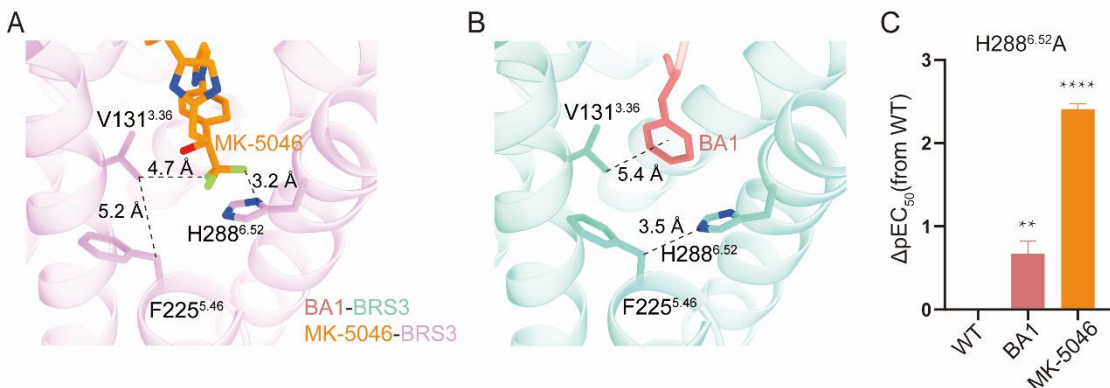
740 **Figure 3. The MK-5046-binding pocket in BRS3.**

741 (A) The chemical structure of MK-5046 and detailed interactions between MK-5046
742 and BRS3.

743 (B) The structural comparison of BA1-BRS3 and MK-5046-BRS3 complexes. The
744 binding site and pose of MK-5046 closely resemble the C-terminal dumbbell end
745 HFX(8-10)^{BA1} motif of BA1.
746 (C and D) Detailed interactions of MK-5046 with BRS3. Hydrogen bonds are depicted
747 as black dashed lines.
748 (E and F) Effects of mutations in the MK-5046-binding pocket in IP1 assay. Data are
749 presented as mean ± S.E.M. of at least three independent experiments. Source data
750 are available online.

751
752
753
754
755
756
757
758
759
760
761
762
763
764
765
766
767
768
769
770
771
772
773
774
775
776
777

Figure 4



778

779 **Figure 4. Activation of BRS3 by agonists of different types**

780 (A and B) The representative structures revealed the difference in the MK-5046-
781 BRS3 (A) and BA1-BRS3 (B) complexes.
782 (C) Effects of H288^{6.52}A on the potency in IP-1 assay. Data were shown as ΔpEC₅₀ ±
783 S.E.M. from three independent experiments, which performed in triplicates, with total
784 repeats of nine for each data point. Statistical differences between wild type (WT)
785 and mutants were determined by two-sided, one-way analysis of variance (ANOVA)
786 with Tukey test. *, P < 0.05; **, P < 0.01; ***, P < 0.001; ns, no significant difference.

787

788

789

790

791

792

793

794

795

796

797

798

799

800

801

802

803

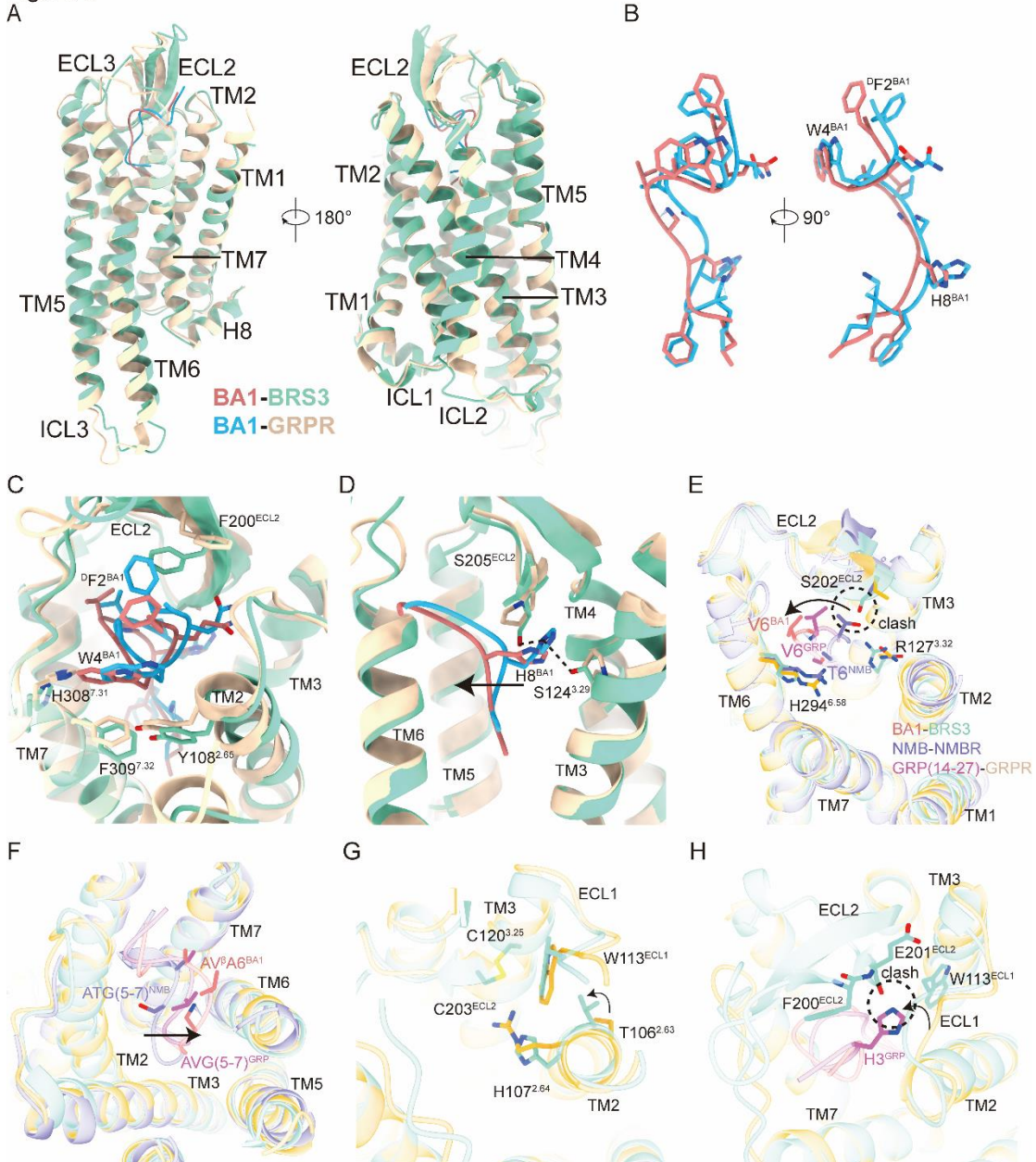
804

805

806

807

Figure 5



808

809 **Figure 5. Molecular basis of ligands selectivity of bombesin receptors.**

810 (A) A structural comparison of BA1-BRS3 and BA1-GRPR complexes. The BA1 in
811 BA1-BRS3 complex is shown in light salmon; the receptor BRS3 is displayed in
812 aquamarine; the BA1 in BA1-GRPR complex is shown in dodger blue; the receptor
813 GRPR is displayed in burly wood.

814 (B) A structural comparison of BA1 conformation in BA1-BRS3 and BA1-GRPR
815 complexes.

816 (C and D) Detailed interactions between ^DF₂^{BA1}, W₄^{BA1}(C), and H₈^{BA1} (D) with
817 residues in GRPR and BRS3. The shift of middle AV^βA(5-7)^{BA1} motif is represented

818 by an arrow.

819 (E) Detailed interactions between T6^{NMB}, V6^{GRP}, and V6^{BA1} with residues in NMBR,
820 GRPR and BRS3. The shift of T6^{NMB} is represented by an arrow.

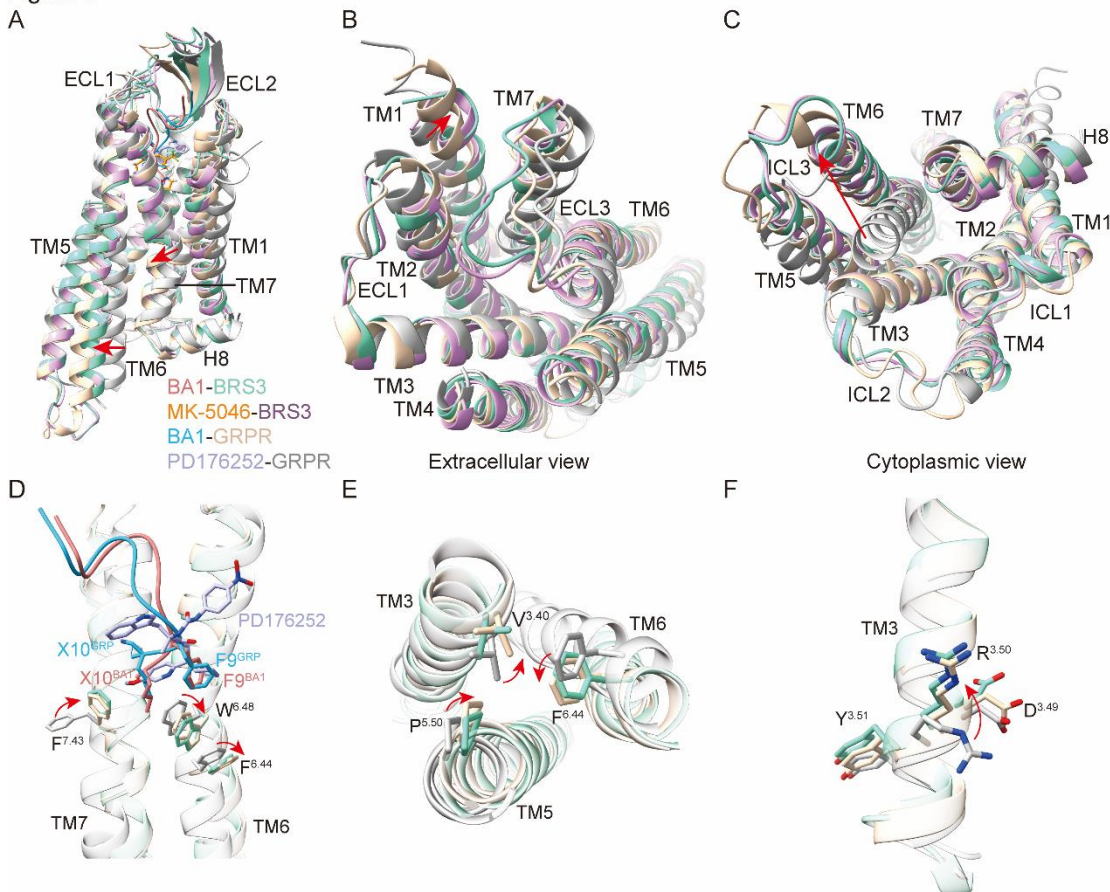
821 (F) Detailed interactions between L3^{NMB}, H3^{GRP}, and Q3^{BA1} with residues in NMBR,
822 GRPR and BRS3. The middle motif of BA1 and GRP exhibits a closer alignment with
823 TM6, and the counterpart of NMB closed to TM2.

824 (G) The inward push of the side chain of W113^{ECL1} by T106^{2.63} substitution and the
825 packing between the side chain of W113^{ECL1} and the H107^{2.64} substitution in BRS3.

826 (H) The clash between H3^{GRP} of GPR(14-27) and EGW(111-113)^{ECL1} of BRS3 is
827 represented by a circle.

828
829
830
831
832
833
834
835
836
837
838
839
840
841
842
843

Figure 6



844

845 **Figure 6. Molecular basis for activation of BRS3.**

846 (A-C) Structural alignment of two active BRS3 in the presence of the ligands BA1 and
 847 MK-5046, active BA1-GRPR (PDB code: 7W40) and inactive GRPR (PDB code:
 848 7W41). Side view (A); extracellular view (B); cytoplasmic view (C). The movement
 849 directions of TM6 and TM7 in BRS3 relative to inactive GRPR are highlighted as red
 850 arrows. Inactive GRPR, active GRPR, active BRS3 in the presence of the ligands
 851 BA1 and MK-5046 are colored in gray, burly wood, aquamarine and violet,
 852 respectively.

853 (D-F) Conformational changes of the conserved 'micro-switches' upon receptor
 854 activation, including toggle switch (D), PV(I)F (E), and DRY(F) motifs. The
 855 conformational changes of residue side chains are shown as red arrows upon
 856 receptor activation. The complex structures were aligned by the receptors.

857

858

859

860 **Methods**
861 **Constructs**

862 Human BRS3(residues 1-361) was cloned into pFastBac with an N-terminal
863 haemagglutinin (HA) signal peptide followed by thermostabilized apocytochrome
864 b₅₆₂RIL (BRIL)¹. LgBiT was also inserted at the C terminus of the BRS3 using
865 homologous recombination (CloneExpress One Step Cloning Kit, Vazyme). After
866 LgBiT, a tobacco etch virus (TEV) protease cleavage site and a double maltose
867 binding protein (MBP) tag were added to BRS3 constructs for improved expression
868 and purification. The engineered Gα_q construct was generated based on mini-G_{s/q}71²,
869 which carries two dominant-negative mutations (G203A and A326S)³ to decrease
870 nucleotide binding affinity and facilitate Gαβγ complex stability. The N-terminal 1-18
871 amino acids and the α-helical domain of the mini-G_{s/q}71 were substituted with the
872 corresponding sequences of the human Gai1 for binding to the antibody fragments
873 scFv16^{4,5}. Rat Gβ1 was connected with a C-terminal HiBiT by a 15 residues linker.
874 The engineered Gα_q, Gβ1-HiBiT and bovine Gγ2 were cloned independently into
875 pFastBac vectors (Invitrogen). The antibody fragment scFv16 was cloned into a
876 modified pFastBac vector containing an N-terminal GP67 secretion signal peptide.

877

878 **Expression and purification of Nb35**

879 Nanobody-35 (Nb35) with a N-terminal pelB signal peptide and a C-terminal His₆ tag
880 was expressed in the periplasm of Escherichia coli BL21(DE3) bacteria (NEB)⁶.
881 Cultures were grown at 37 °C in Luria-Bertani media containing 50 µg/mL ampicillin
882 to an OD₆₀₀ of 1.0 and induced with 0.1mM IPTG at 28 °C, 180 r.p.m. for another 8 h.
883 Cells were harvested by centrifugation (5316 × g, 30 min) and lysed in ice-cold buffer
884 (20mM HEPES pH 7.4, 500mM NaCl), then centrifuged to remove cell debris. Nb35
885 was first purified by nickel affinity chromatography, followed by size-exclusion
886 chromatography using a HiLoad 16/600 Superdex 200 prep grade column with a
887 buffer of 20mM HEPES pH 7.4 and 100mM NaCl. Peak fractions were concentrated
888 to 2mg/mL with 15% glycerol and kept frozen at -80 °C for later use. Purified protein
889 quality was assessed by SDS-PAGE.

890

891 **Expression and purification of complexes**

892 High Five cells (Expression systems) were cultured in ESF921 serum-free medium
893 (Expression Systems) and co-infected with baculoviruses expressing the receptor,
894 G α _q, G β 1, G γ 2, and scFv16⁷ at a 1:1:1:1 ratio for 48 h at 27 °C using Bac-to-Bac
895 baculovirus system. The cell pellets were lysed by dounce homogenization in a buffer
896 containing 20 mM HEPES pH 7.4, 100 mM NaCl, 10 mM MgCl₂, 0.1 mM TCEP
897 (Sigma-Aldrich), 10% glycerol, and EDTA-free protease inhibitor cocktail (TargetMol).
898 The supernatant was isolated by centrifugation at 65,000 × g for 40 minutes to collect
899 the membranes. The washed membranes were resuspended in buffer containing 20
900 mM HEPES pH 7.4, 100 mM NaCl, 10 mM MgCl₂, 10% glycerol, agonists (10 μ M
901 BA1, and 10 μ M MK-5046, Synpeptide and MedChemExpress, respectively), 25
902 mU/mL apyrase (Sigma-Aldrich), 20ug/mL Nb35, 0.1 mM TCEP and EDTA-free
903 protease inhibitor cocktail, and incubated at 4 °C for 8 hours. After incubation, cell
904 membranes were solubilized with 1% (w/v) n-dodecyl- β -D-maltopyranoside (DDM,
905 Anatrace) and 0.2% (w/v) cholesteryl hemisuccinate TRIS salt (CHS, Anatrace) at
906 4 °C for 2 hours. The supernatant was collected by centrifugation at 65,000 × g for 35
907 minutes and incubated with dextrin resin (Dextrin Beads 6FF, Smart Life Sciences) at
908 4 °C for 5 hours. The resin was washed, eluted, and the protein complexes were
909 further purified by size-exclusion chromatography on a Superdex 200 increase
910 10/300 GL column (GE Healthcare) in buffer containing 20 mM HEPES pH 7.4, 100
911 mM NaCl, 2 mM MgCl₂, 0.1 mM TCEP, agonists (10 μ M BA1, 10 μ M MK5046, and 1
912 mM oridonin), 0.00075%(w/v) LMNG, 0.00025% (w/v) GDN and 0.0002% (w/v) CHS.
913 Fractions containing monomeric protein complex were collected and evaluated by
914 SDS-PAGE ([Figure S2](#)), and then concentrated by 30-fold for cryo-electron
915 microscopy experiments.

916

917 **Cryo-EM data collection**

918 Cryo-EM grids were prepared with the Vitrobot Mark IV plunger (FEI) set to 8 °C and
919 100% humidity. Three-microliter of the BRS3-G α _q protein complex in apo state was

920 applied to the glow discharged copper R1.2/1.3 holey carbon grids. The sample was
921 incubated for 10 s on the grids before blotting for 3.5 s (double-sided, blot force 1) and
922 flash-frozen in liquid ethane immediately. The same condition was used for the sample
923 BA1-BRS3-G_q complex, and MK5046-BRS3-G_q complex.

924

925 For BRS3-G_q complex dataset, 3,098 movies were collected on a Titan Krios equipped
926 with a Gatan K3 direct electron detection device at 300 kV with a magnification of
927 64,000, corresponding to a pixel size 1.08 Å. Image acquisition was performed with
928 EPU Software (FEI Eindhoven, Netherlands). We collected a total of 36 frames
929 accumulating to a total dose of 50 e⁻ Å⁻² over 2.5 s exposure.

930

931 For BA1-BRS3-G_q complex dataset, 5,016 movies were collected on a Titan Krios
932 equipped with a Gatan K3 direct electron detection device at 300 kV with a
933 magnification of 105,000, corresponding to a pixel size 0.824 Å. Image acquisition was
934 performed with EPU Software (FEI Eindhoven, Netherlands). We collected a total of
935 36 frames accumulating to a total dose of 50 e⁻ Å⁻² over 2.5 s exposure.

936

937 For MK5046-BRS3-G_q complex dataset, 8,738 movies were collected on a Titan Krios
938 equipped with a Falcon4 direct electron detection device at 300 kV with a magnification
939 of 165,000, corresponding to a pixel size 0.73 Å. Image acquisition was performed with
940 EPU Software (FEI Eindhoven, Netherlands). We collected a total dose of 50 e⁻ Å⁻²
941 over 2.5 s exposure on each EER format movie⁸. Each movie was divided into 36
942 frames during motion correction.

943

944 **Cryo-EM image processing**

945 MotionCor2 was used to perform the frame-based motion-correction algorithm to
946 generate drift-corrected micrograph for further processing, and CTFFIND4 provided
947 the estimation of the contrast transfer function (CTF) parameters^{9,10}.

948

949 For BRS3-G_q complex dataset, approximately 2,000 particles were manually picked
950 and two-dimensional (2D) classes were calculated and used as references for
951 automatic picking. All subsequent steps including particle picking and extraction, 2D
952 classification, three-dimensional (3D) classification, 3D refinement, CTF refinement,
953 Bayesian polishing, post processing and local resolution estimation were performed
954 using Relion3.0¹¹.

955

956 A total of 3,294,877 particles were extracted from the cryo-EM micrographs and
957 followed by two rounds of reference-free 2D classification, yielding 3,270,779 particles
958 after clearance. Three rounds of 3D classification were used to separate out 233,381
959 particles, which were refined to a structure at 3.93 Å global resolution. After CTF
960 refinement, polishing, and postprocessing, the particles were reconstituted to a 3.29 Å
961 structure. ([Figure S3](#); [Table S2](#)).

962

963 For BA1-BRS3-G_q complex dataset, the subsequent steps were performed with
964 CryoSPARC¹². Blob-pick was used for the particle picking. 6,245,406 particles were
965 automatic picked and extracted from 5,016 cryo-EM micrographs. After 2 rounds of 2D
966 classification, 799,895 particles were selected from 2,116,883 particles and subjected
967 to generate 5 “good” references and 1,040,145 particles were selected and subjected
968 to generate 5 “bad” references. Two rounds of heterogeneous refinement using “good”
969 and “bad” references yielded 675,060 particles after clearance. We then continued the
970 processing in CryoSPARC. After homogeneous refinement and non-uniform
971 refinement, the particles were reconstituted to a 2.90 Å structure ([Figure S4](#); [Table S2](#)).

972

973 For datasets of MK-5046-BRS3-G_q complex, the similar strategy was used. After non-
974 uniform refinement, 196,746 particles were reconstituted to 2.93 Å structure, which
975 corresponding to MK-5046-BRS3-G_q complex ([Figure S5](#); [Table S2](#)).

976

977 **Model building**

978 BRS3 structure predicted from Alphafold2 was used as the starting reference models
979 for receptors building¹³. Structures of Gα_q, Gβ, Gγ, the NB35 nanobody, and scFv16
980 derived from PDB entry 8H0Q¹⁴ were rigid body fit into the density. All models were
981 fitted into the EM density map using UCSF Chimera¹⁵ followed by iterative rounds of
982 manual adjustment and automated rebuilding in COOT¹⁶ and PHENIX¹⁷, respectively.
983 The models were adjusted in ISOLDE¹⁸ followed by refinement in PHENIX. The final
984 model statistics were validated using Comprehensive validation (cryo-EM) in
985 PHENIX¹⁷ and provided in the **Table S2**. All structural figures were prepared using
986 Chimera¹⁵, Chimera X¹⁹, and PyMOL (Schrödinger, LLC.).

987

988 **Function assay**

989 AD293 cells (Agilent) were cultured in high glucose DMEM medium (GE healthcare)
990 supplemented with 10% (v/v) fetal bovine serum (FBS, Gemini) and 1%
991 penicillin/streptomycin at 37°C in 5% CO₂ incubator. Inositol phosphate 1 (IP1)
992 production was measured using the IP-One HTRF kit (Cisbio, 621PAPEJ)²⁰. Briefly,
993 cells were seeded onto 12-well plates 16 hours before transfection. Cells were then
994 transiently with different BRS3 constructs using FuGENE HD transfection reagent.
995 After 24 hours, cells were harvested and resuspended at 7 × 10⁵ cells/mL in IP1
996 stimulation buffer. Cells were then plated onto 384-well assay plates at 4,900 cells/7
997 μL/well. 7 μL IP1 Stimulation Buffer 2 containing ligand was added and incubated for
998 1 hour at 37 °C. Intracellular IP1 was measured using the IP-One HTRF kit and an
999 EnVision multiplate reader according to the manufacturer's protocol. The HTRF ratio
1000 was converted to a response (%) using: response (%) = ratio of sample/WT×100.
1001 Data presented are mean ± S.E.M. of at least three independently biological
1002 experiments.

1003

1004 **Cell-surface expression assay**

1005 Cell-surface expression for each BRS3 mutant was monitored by a fluorescence-
1006 activated cell sorting (FACS). The mutants were cloned into pcDNA6.0 vector

1007 (Invitrogen) with a N-terminal FLAG tag. Cells were seeded and transfected as
1008 described for the functional assay. After 24 hours of transfection, cells were washed
1009 with PBS and detached with 0.2% (w/v) EDTA in PBS. The expressed cells were
1010 then incubated with monoclonal anti-FLAG M2-FITC (Sigma-Aldrich) at 1:100 dilution
1011 for 15 minutes at 4 °C, followed by a 9-fold excess of PBS. Cells were resuspended
1012 and fluorescence intensity was quantified using a BD Accuri C6 flow cytometer (BD
1013 Biosciences) with 488 nm excitation and 519 nm emission. FACS data were
1014 analyzed with BD Accuri C6 software 1.0.264.21 and normalized to wild-type BRS3.

1015

1016 **Computational methods**

1017 The simulation systems come from MK-5046-BRS3-G protein complex and BA1-
1018 BRS3-G protein complex. G proteins were removed before simulations. Protonation
1019 states of residues were determined using Propka3 software²¹. The CHARMM-GUI
1020 platform facilitated embedding of these structures into a 75x75 Å POPC lipid bilayer²².
1021 The lipid bilayer was then surrounded by a 15 Å aqueous layer. Systems were then
1022 adjusted to a 0.15 mol/L NaCl concentration, supplemented with counterions. We
1023 applied the CHARMM36m force field for amino acids and lipids, while CHARMM
1024 general force field is applied for ligands^{23,24}. The systems underwent a 7-step
1025 equilibration process, with gradual minimization and relaxation of constraints, as
1026 outlined by CHARMM-GUI. We conducted 3×500 ns independent production runs for
1027 each system using pmemd.cuda in Amber20²⁵ under the NPT ensemble at 303.15 K
1028 and 1 atm. Long-range electrostatics were managed via the Particle Mesh Ewald
1029 method, while short-range electrostatic and van der Waals interactions used a 12 Å
1030 cutoff, with a smooth transition between 10 and 12 Å. The hydrophobic network was
1031 evaluated using “nativecontact” command in CPPTRAJ. The interacting interface area
1032 was calculated using dr_sasa²⁶.

1033

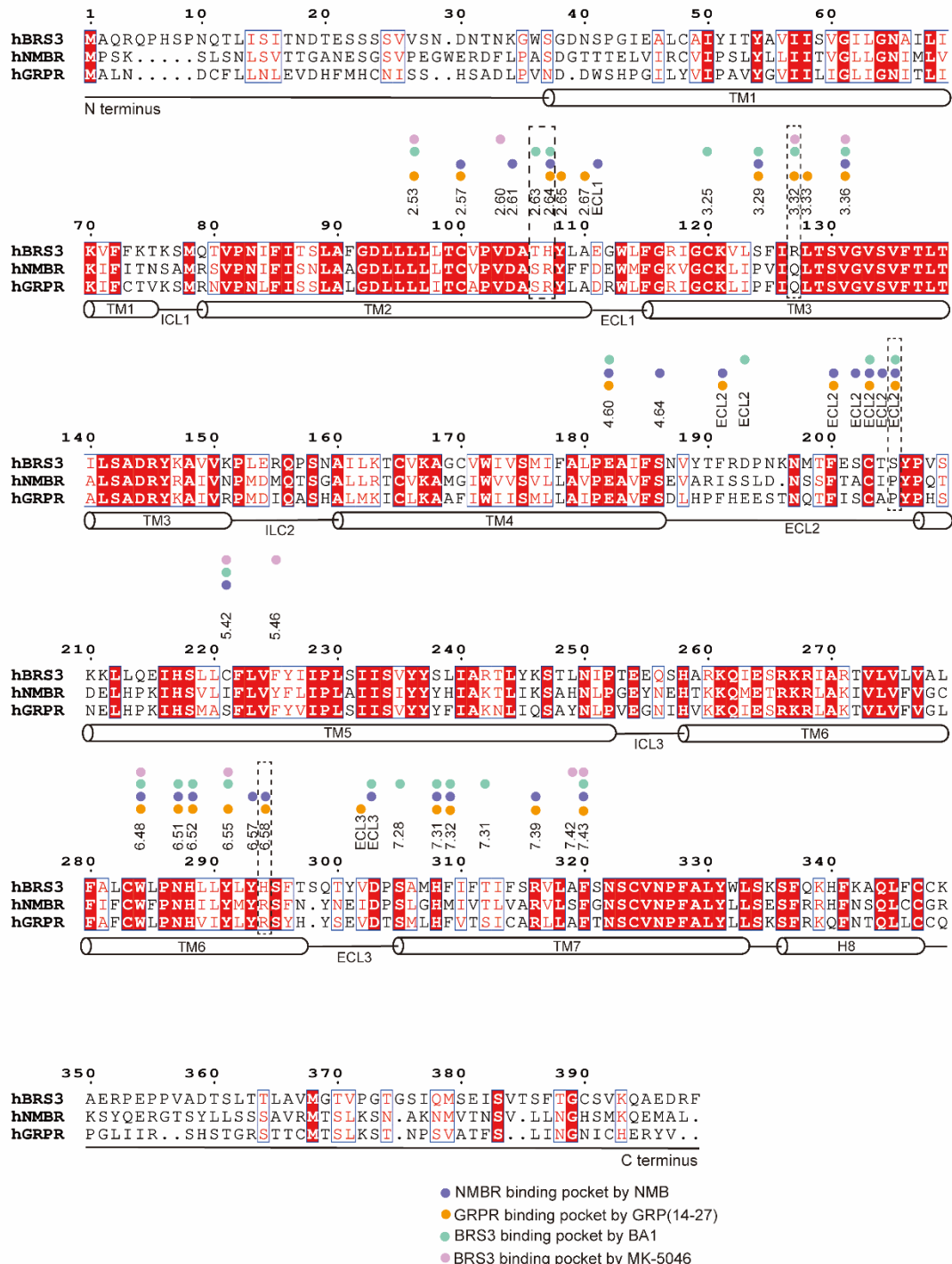
1034 **Reference**

- 1035 1. Chun, E., Thompson, A.A., Liu, W., Roth, C.B., Griffith, M.T., Katritch, V., Kunken, J., Xu, F.,
1036 Cherezov, V., Hanson, M.A., and Stevens, R.C. (2012). Fusion Partner Toolchest for the
1037 Stabilization and Crystallization of G Protein-Coupled Receptors. *Structure* 20, 967-976.

- 1038 10.1016/j.str.2012.04.010.
- 1039 2. Nehme, R., Carpenter, B., Singhal, A., Strege, A., Edwards, P.C., White, C.F., Du, H.,
1040 Grisshammer, R., and Tate, C.G. (2017). Mini-G proteins: Novel tools for studying GPCRs
1041 in their active conformation. *PLoS One* *12*, e0175642. 10.1371/journal.pone.0175642.
- 1042 3. Liu, P., Jia, M.Z., Zhou, X.E., De Waal, P.W., Dickson, B.M., Liu, B., Hou, L., Yin, Y.T., Kang,
1043 Y.Y., Shi, Y., et al. (2016). The structural basis of the dominant negative phenotype of the
1044 Galphai1beta1gamma2 G203A/A326S heterotrimer. *Acta Pharmacol Sin* *37*, 1259-1272.
1045 10.1038/aps.2016.69.
- 1046 4. Maeda, S., Qu, Q., Robertson, M.J., Skiniotis, G., and Kobilka, B.K. (2019). Structures of the
1047 M1 and M2 muscarinic acetylcholine receptor/G-protein complexes. *Science* *364*, 552-
1048 557. 10.1126/science.aaw5188.
- 1049 5. Kang, Y., Kuybeda, O., de Waal, P.W., Mukherjee, S., Van Eps, N., Dutka, P., Zhou, X.E.,
1050 Bartesaghi, A., Erramilli, S., Morizumi, T., et al. (2018). Cryo-EM structure of human
1051 rhodopsin bound to an inhibitory G protein. *Nature* *558*, 553-558. 10.1038/s41586-018-
1052 0215-y.
- 1053 6. Rasmussen, S.G., Choi, H.J., Fung, J.J., Pardon, E., Casarosa, P., Chae, P.S., Devree, B.T.,
1054 Rosenbaum, D.M., Thian, F.S., Kobilka, T.S., et al. (2011). Structure of a nanobody-
1055 stabilized active state of the beta(2) adrenoceptor. *Nature* *469*, 175-180.
1056 10.1038/nature09648.
- 1057 7. Maeda, S., Koehl, A., Matile, H., Hu, H., Hilger, D., Schertler, G.F.X., Manglik, A., Skiniotis,
1058 G., Dawson, R.J.P., and Kobilka, B.K. (2018). Development of an antibody fragment that
1059 stabilizes GPCR/G-protein complexes. *Nat Commun* *9*, 3712. 10.1038/s41467-018-
1060 06002-w.
- 1061 8. Guo, H., Franken, E., Deng, Y., Benlekbir, S., Singla Lezcano, G., Janssen, B., Yu, L., Ripstein,
1062 Z.A., Tan, Y.Z., and Rubinstein, J.L. (2020). Electron-event representation data enable
1063 efficient cryoEM file storage with full preservation of spatial and temporal resolution. *IUCrJ*
1064 *7*, 860-869. 10.1107/S205225252000929X.
- 1065 9. Zheng, S.Q., Palovcak, E., Armache, J.P., Verba, K.A., Cheng, Y., and Agard, D.A. (2017).
1066 MotionCor2: anisotropic correction of beam-induced motion for improved cryo-electron
1067 microscopy. *Nat Methods* *14*, 331-332. 10.1038/nmeth.4193.
- 1068 10. Rohou, A., and Grigorieff, N. (2015). CTFFIND4: Fast and accurate defocus estimation from
1069 electron micrographs. *J Struct Biol* *192*, 216-221. 10.1016/j.jsb.2015.08.008.
- 1070 11. Zivanov, J., Nakane, T., Forsberg, B.O., Kimanis, D., Hagen, W.J.H., Lindahl, E., and Scheres,
1071 S.H.W. (2018). New tools for automated high-resolution cryo-EM structure determination
1072 in RELION-3. *eLife* *7*. ARTN e4216610.7554/eLife.42166.
- 1073 12. Punjani, A., Rubinstein, J.L., Fleet, D.J., and Brubaker, M.A. (2017). cryoSPARC: algorithms
1074 for rapid unsupervised cryo-EM structure determination. *Nat Methods* *14*, 290-296.
1075 10.1038/nmeth.4169.
- 1076 13. Tunyasuvunakool, K., Adler, J., Wu, Z., Green, T., Zielinski, M., Zidek, A., Bridgland, A., Cowie,
1077 A., Meyer, C., Laydon, A., et al. (2021). Highly accurate protein structure prediction for the
1078 human proteome. *Nature* *596*, 590-596. 10.1038/s41586-021-03828-1.
- 1079 14. Zhuang, Y., Xu, P., Mao, C., Wang, L., Krumm, B., Zhou, X.E., Huang, S., Liu, H., Cheng, X.,
1080 Huang, X.P., et al. (2021). Structural insights into the human D1 and D2 dopamine receptor
1081 signaling complexes. *Cell* *184*, 931-942 e918. 10.1016/j.cell.2021.01.027.

- 1082 15. Pettersen, E.F., Goddard, T.D., Huang, C.C., Couch, G.S., Greenblatt, D.M., Meng, E.C., and
1083 Ferrin, T.E. (2004). UCSF Chimera--a visualization system for exploratory research and
1084 analysis. *J Comput Chem* *25*, 1605-1612. 10.1002/jcc.20084.
- 1085 16. Emsley, P., and Cowtan, K. (2004). Coot: model-building tools for molecular graphics. *Acta*
1086 *Crystallogr D Biol Crystallogr* *60*, 2126-2132. 10.1107/S0907444904019158.
- 1087 17. Adams, P.D., Gopal, K., Grosse-Kunstleve, R.W., Hung, L.W., Ioerger, T.R., McCoy, A.J.,
1088 Moriarty, N.W., Pai, R.K., Read, R.J., Romo, T.D., et al. (2004). Recent developments in the
1089 PHENIX software for automated crystallographic structure determination. *J Synchrotron*
1090 *Radiat* *11*, 53-55. 10.1107/s0909049503024130.
- 1091 18. Croll, T.I. (2018). ISOLDE: a physically realistic environment for model building into low-
1092 resolution electron-density maps. *Acta Crystallogr D Struct Biol* *74*, 519-530.
1093 10.1107/S2059798318002425.
- 1094 19. Pettersen, E.F., Goddard, T.D., Huang, C.C., Meng, E.C., Couch, G.S., Croll, T.I., Morris, J.H.,
1095 and Ferrin, T.E. (2021). UCSF ChimeraX: Structure visualization for researchers, educators,
1096 and developers. *Protein Sci* *30*, 70-82. 10.1002/pro.3943.
- 1097 20. Leyris, J.P., Roux, T., Trinquet, E., Verdie, P., Fehrentz, J.A., Oueslati, N., Douzon, S., Bourrier,
1098 E., Lamarque, L., Gagne, D., et al. (2011). Homogeneous time-resolved fluorescence-
1099 based assay to screen for ligands targeting the growth hormone secretagogue receptor
1100 type 1a. *Anal Biochem* *408*, 253-262. 10.1016/j.ab.2010.09.030.
- 1101 21. Olsson, M.H.M., Søndergaard, C.R., Rostkowski, M., and Jensen, J.H. (2011). PROPKA3:
1102 Consistent Treatment of Internal and Surface Residues in Empirical pKa Predictions.
1103 *Journal of Chemical Theory and Computation* *7*, 525-537. 10.1021/ct100578z.
- 1104 22. Wu, E.L., Cheng, X., Jo, S., Rui, H., Song, K.C., Dávila-Contreras, E.M., Qi, Y., Lee, J., Monje-
1105 Galvan, V., Venable, R.M., et al. (2014). CHARMM-GUI Membrane Builder toward realistic
1106 biological membrane simulations. *J Comput Chem* *35*, 1997-2004. 10.1002/jcc.23702.
- 1107 23. Huang, J., Rauscher, S., Nawrocki, G., Ran, T., Feig, M., de Groot, B.L., Grubmüller, H., and
1108 MacKerell, A.D. (2017). CHARMM36m: an improved force field for folded and intrinsically
1109 disordered proteins. *Nat. Methods* *14*, 71-73. 10.1038/nmeth.4067.
- 1110 24. Vanommeslaeghe, K., Hatcher, E., Acharya, C., Kundu, S., Zhong, S., Shim, J., Darian, E.,
1111 Guvench, O., Lopes, P., Vorobyov, I., and Mackerell, A.D., Jr. (2010). CHARMM general
1112 force field: A force field for drug-like molecules compatible with the CHARMM all-atom
1113 additive biological force fields. *J Comput Chem* *31*, 671-690. 10.1002/jcc.21367.
- 1114 25. Salomon-Ferrer, R., Götz, A.W., Poole, D., Le Grand, S., and Walker, R.C. (2013). Routine
1115 Microsecond Molecular Dynamics Simulations with AMBER on GPUs. 2. Explicit Solvent
1116 Particle Mesh Ewald. *J Chem Theory Comput* *9*, 3878-3888. 10.1021/ct400314y.
- 1117 26. Ribeiro, J., Ríos-Vera, C., Melo, F., and Schüller, A. (2019). Calculation of accurate
1118 interatomic contact surface areas for the quantitative analysis of non-bonded molecular
1119 interactions. *Bioinformatics* *35*, 3499-3501. 10.1093/bioinformatics/btz062.
- 1120
1121
1122
1123
1124
1125

Figure S1



1127

1128

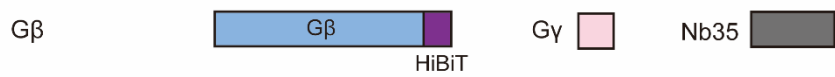
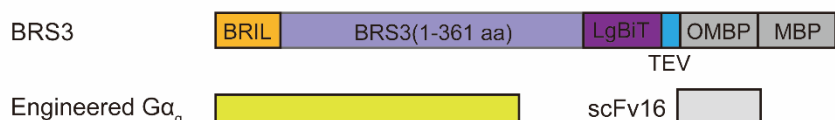
1129 **Figure S1. Sequence alignment of BRS3, NMBR, and GRPR.** Secondary structure

elements are annotated underneath the sequences based on the structure of the BRS3-G_q complex. The ligand-binding pockets of NMB-NMBR, GRP(14-27)-GRPR, BA1-BRS3, and MK-5046-BRS3 is displayed in different colors, purple, orange,

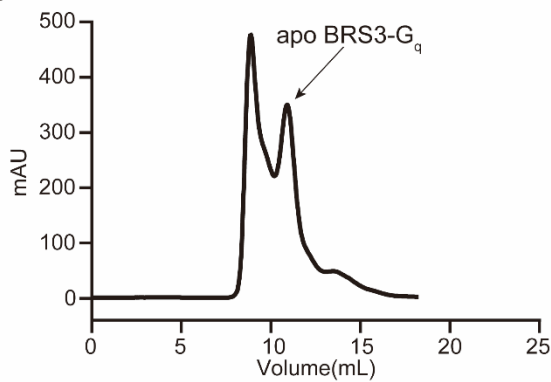
1133 green, and violet, respectively. Additionally, the non-conserved residues including
1134 $S^{2.63}$, $R^{2.64}$, $Q^{3.32}$, $P^{45.52}$, and $R^{6.58}$, is circled in dotted box.

Figure S2

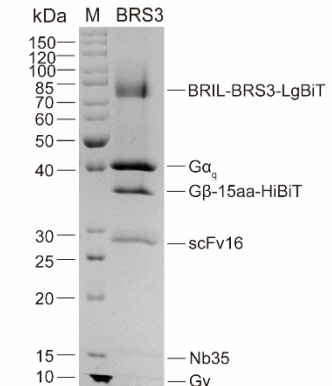
A



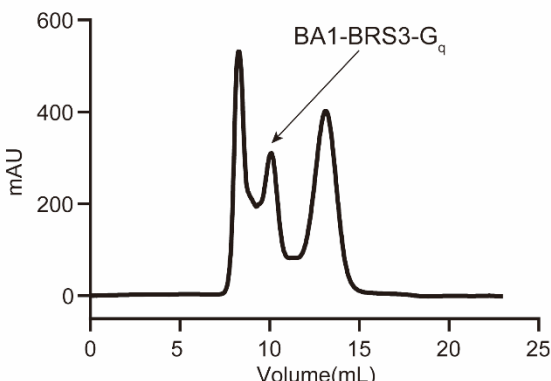
B



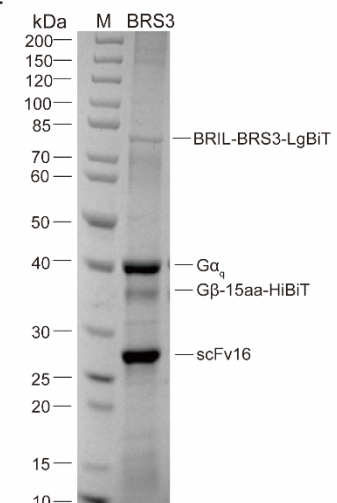
C



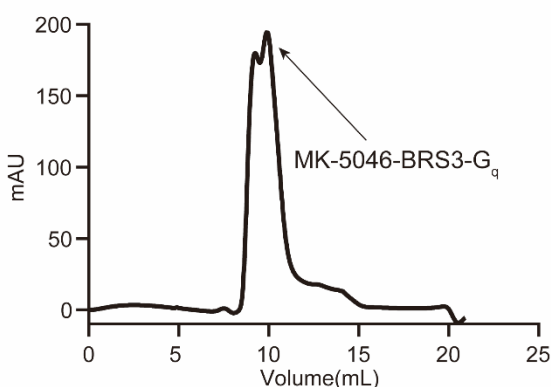
D



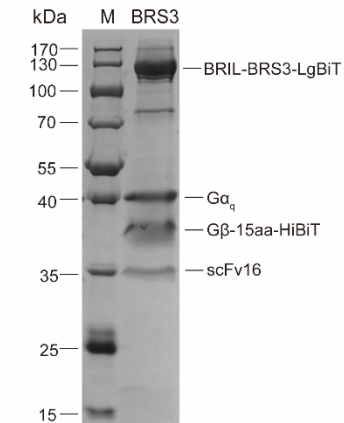
E



F



G



1136 **Figure S2. Purification and characterization of BA1-BRS3-G_q complex and MK-**
1137 **5046-BRS3-G_q complex.**

1138 (A) Schematic diagram of the protein engineering of BRS3, engineered Gα_q, Gβ, Gγ,
1139 scFv16, and Nb35 used in this study.

1140 (B) Gel filtration (Superdex 200 Increase 10/300 column, GE Healthcare) profile of the
1141 apo BRS3–G_q complex. The black arrow indicates the sharp peak for apo BRS3–G_q
1142 complex.

1143 (C) Coomassie-stained SDS-PAGE analysis of the purified apo BRS3–G_q complex,
1144 showing balanced ratios for each subunit.

1145 (D) Gel filtration (Superdex 200 Increase 10/300 column, GE Healthcare) profile of the
1146 BA1-BRS3–G_q complex. The black arrow indicates the sharp peak for BA1-BRS3–G_q
1147 complex.

1148 (E) Coomassie-stained SDS-PAGE analysis of the purified BA1-BRS3–G_q complex,
1149 showing balanced ratios for each subunit.

1150 (F) Gel filtration (Superdex 200 Increase 10/300 column, GE Healthcare) profile of the
1151 MK-5046-BRS3-G_q complex. The black arrow indicates the sharp peak for MK-5046-
1152 BRS3-G_q complex.

1153 (G) Coomassie-stained SDS-PAGE analysis of the purified MK-5046-BRS3-G_q
1154 complex, showing balanced ratios for certain subunits, except for the Gγ subunit.

1155

1156

1157

1158

1159

1160

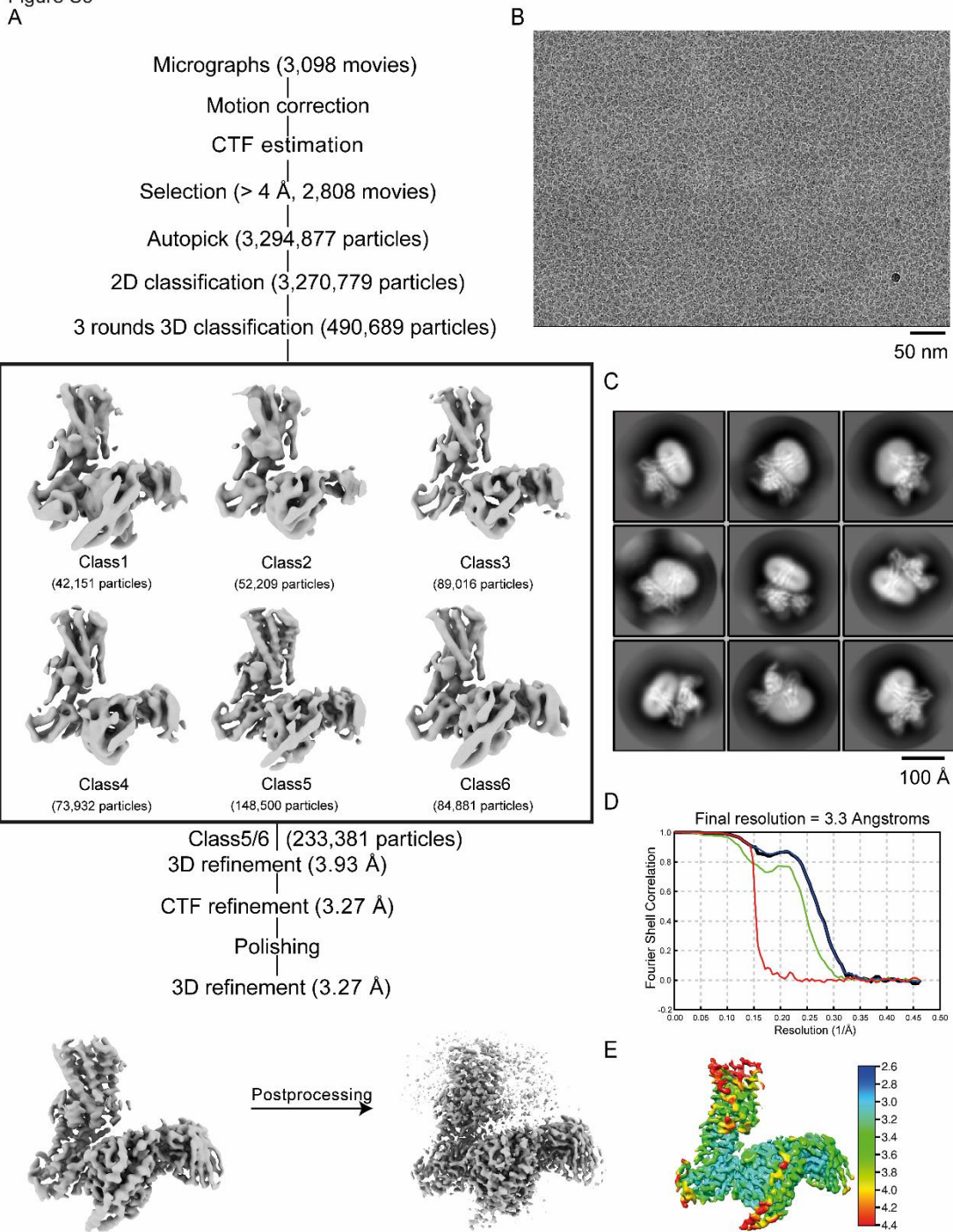
1161

1162

1163

1164

Figure S3



1165

1166

1167 **Figure S3. Cryo-EM data processing of apo BRS3–G_q complex.**

1168 (A) Flowchart of computational sorting of cryo-EM data.

1169 (B) A representative cryo-EM micrograph of apo BRS3–G_q complex with 50 nm scale
1170 bar included as a size reference.

1171 (C) Twelve representative reference-free 2D cryo-EM class averages. Scale bar, 5 nm.

1172 (D) ‘Gold-standard’ Fourier shell correlation curve of the reconstruction. The resolution
1173 was reported at 3.30 Å using the Fourier shell cutoff at 0.143.

1174 (E) Local resolution map of apo BRS3–G_q complex.

1175

1176

1177

1178

1179

1180

1181

1182

1183

1184

1185

1186

1187

1188

1189

1190

1191

1192

1193

1194

1195

1196

Figure S4

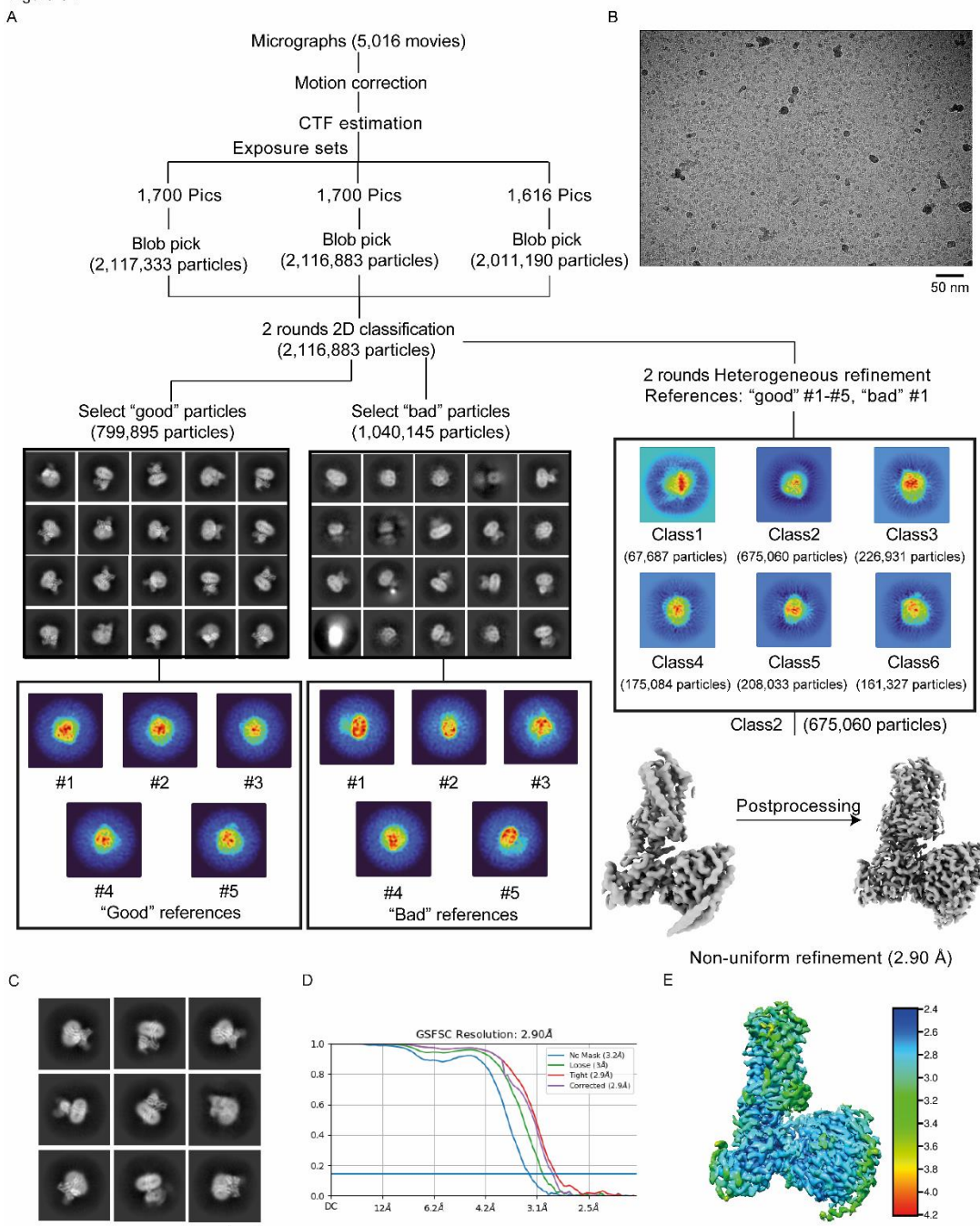


Figure S4. Cryo-EM data processing of BA1-BRS3-G_q complex.

- (A) Flowchart of computational sorting of cryo-EM data.
- (B) A representative cryo-EM micrograph of BA1-BRS3-G_q complex with 50 nm scale bar included as a size reference.
- (C) Twelve representative reference-free 2D cryo-EM class averages. Scale bar, 5 nm.
- (D) 'Gold-standard' Fourier shell correlation curve of the reconstruction. The resolution

1205 was reported at 2.90 Å using the Fourier shell cutoff at 0.143.

1206 (E) Local resolution map of BA1-BRS3–G_q complex.

1207

1208

1209

1210

1211

1212

1213

1214

1215

1216

1217

1218

1219

1220

1221

1222

1223

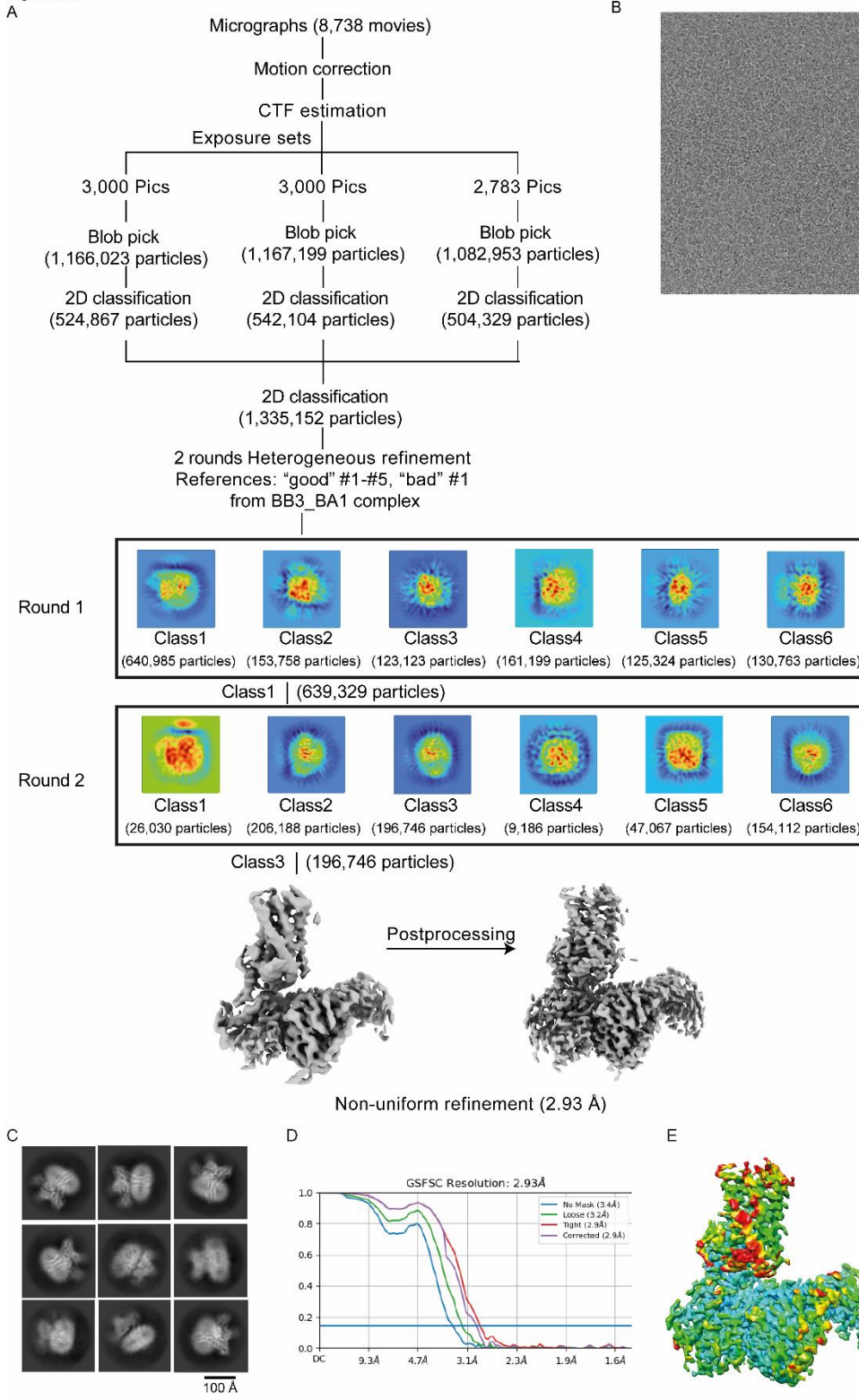
1224

1225

1226

1227

Figure S5

1230 **Figure S5. Cryo-EM data processing of MK-5046-BRS3-G_q complex.**

1231 (A) Flowchart of computational sorting of cryo-EM data.

1232 (B) A representative cryo-EM micrograph of MK-5046-BRS3-G_q complex with 50 nm

1233 scale bar included as a size reference.

1234 (C) Twelve representative reference-free 2D cryo-EM class averages. Scale bar, 5 nm.

1235 (D) 'Gold-standard' Fourier shell correlation curve of the reconstruction. The resolution

1236 as reported at 2.93 Å using the Fourier shell cutoff at 0.143.

1237 (E) Local resolution map of MK-5046-BRS3-G_q complex.

1238

1239

1240

1241

1242

1243

1244

1245

1246

1247

1248

1249

1250

1251

1252

1253

1254

1255

1256

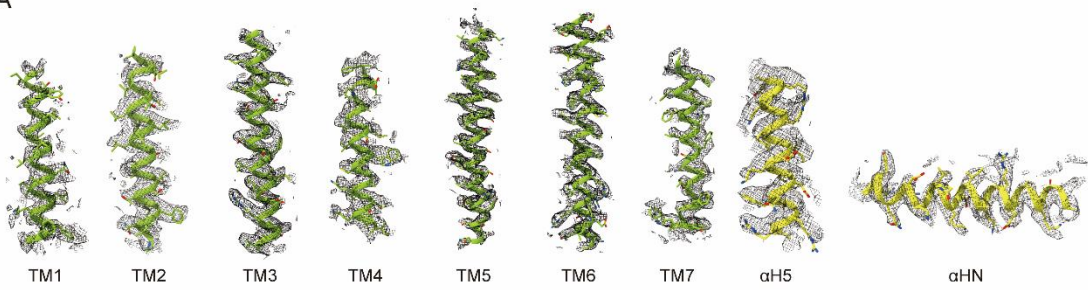
1257

1258

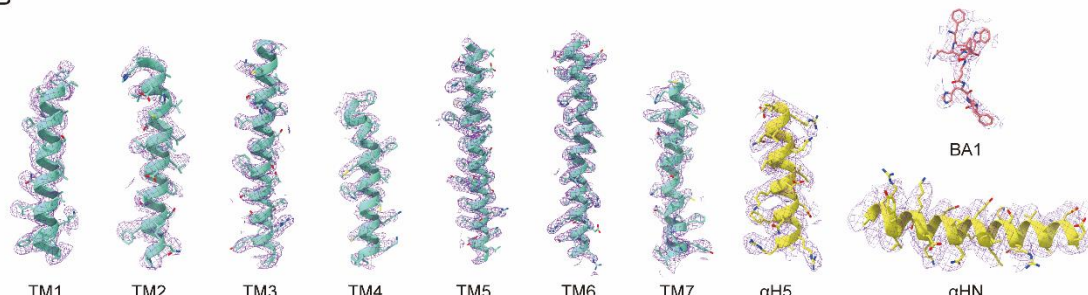
1259

Figure S6

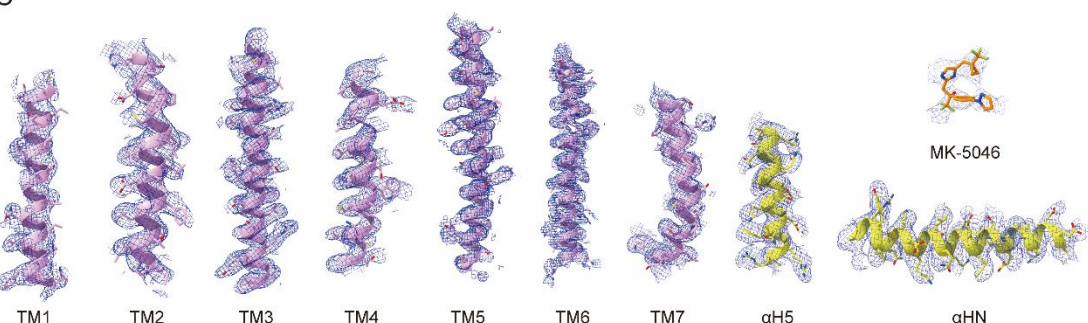
A



B



C



1260

TM1

1261

1262 **Figure S6. Cryo-EM density maps of TM1-7 in receptors, αH5 and αHN in G_q**
1263 **proteins, and ligands in apo BRS3-G_q complex structure(A), BA1-BRS3-G_q**
1264 **complex structure (B), and MK-5046-BRS3-G_q complex structure (C).**

1265

1266

1267

1268

1269

1270

1271

1272

1273

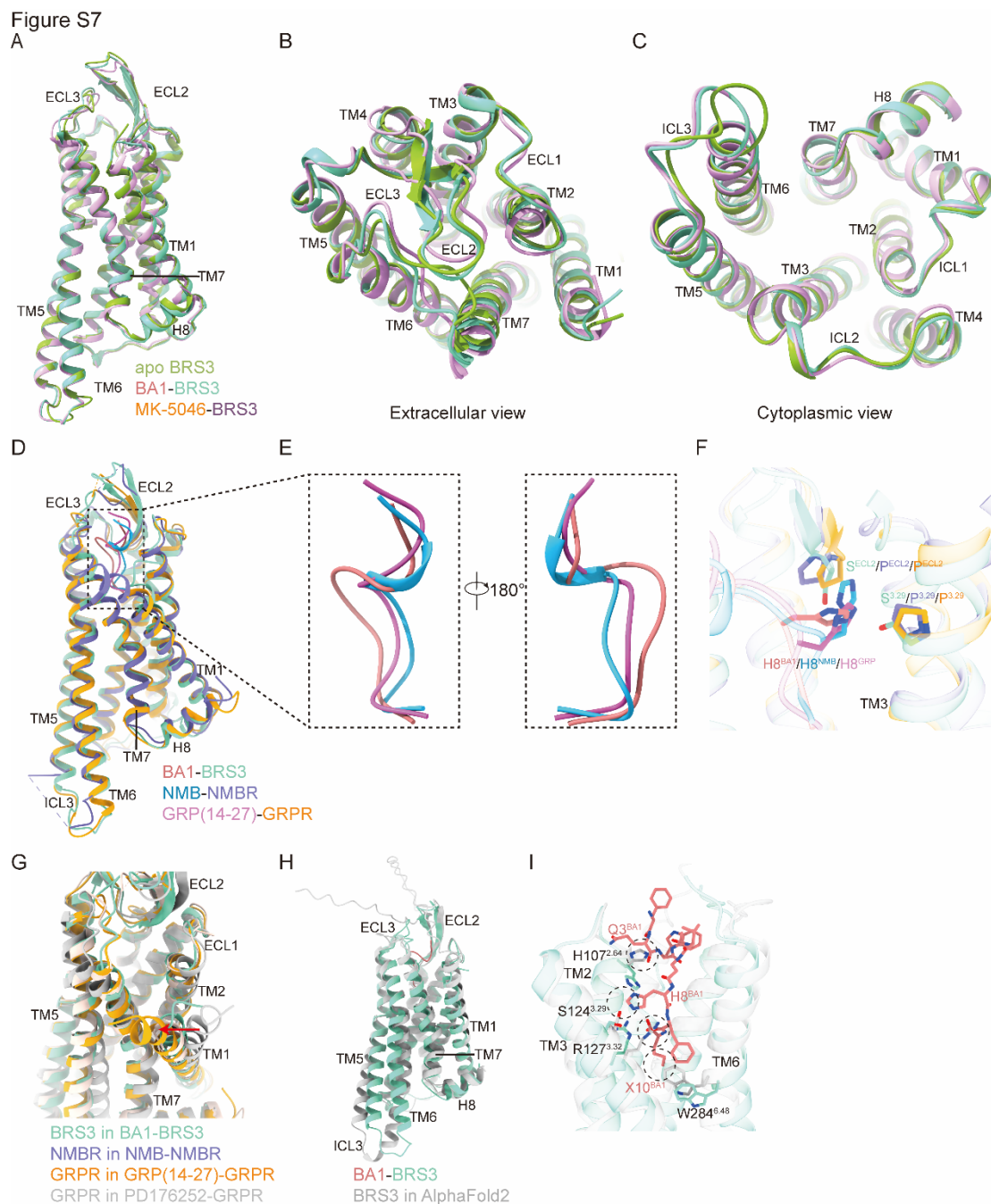


Figure S7. Structural comparison of bombesin receptors family.

(A-C) Different views of the structural superposition of apo-state BRS3 (forest green), BA1-bound BRS3 (medium aquamarine), MK-5046-bound BRS3 (dark khaki).
 (D and E) Side view of the structural superposition of BA1-BRS3, NMB-NMBR, and GRP(14-27)-GRPR(D), and three ligands(E).

1282 (F) The H^{8B} residue forms hydrogen bonds with S124^{3.29} and S205^{ECL2}, differing from
1283 its analogs in NMB and GRP(14-27).

1284 (G) The structural superposition of BRS3 in BA1-BRS3, NMBR in NMB-NMBR, GRPR
1285 in GRP(14-27)-GRPR, and GRPR in PD176252-GRPR.

1286 (H and I) The structural comparison of BRS3 in BA1-BRS3 and AlphaFold2 website(H)
1287 and the clashes between BA1 and OBP in the AlphaFold2 BRS3 structure(I).

1288

1289

1290

1291

1292

1293

1294

1295

1296

1297

1298

1299

1300

1301

1302

1303

1304

1305

1306

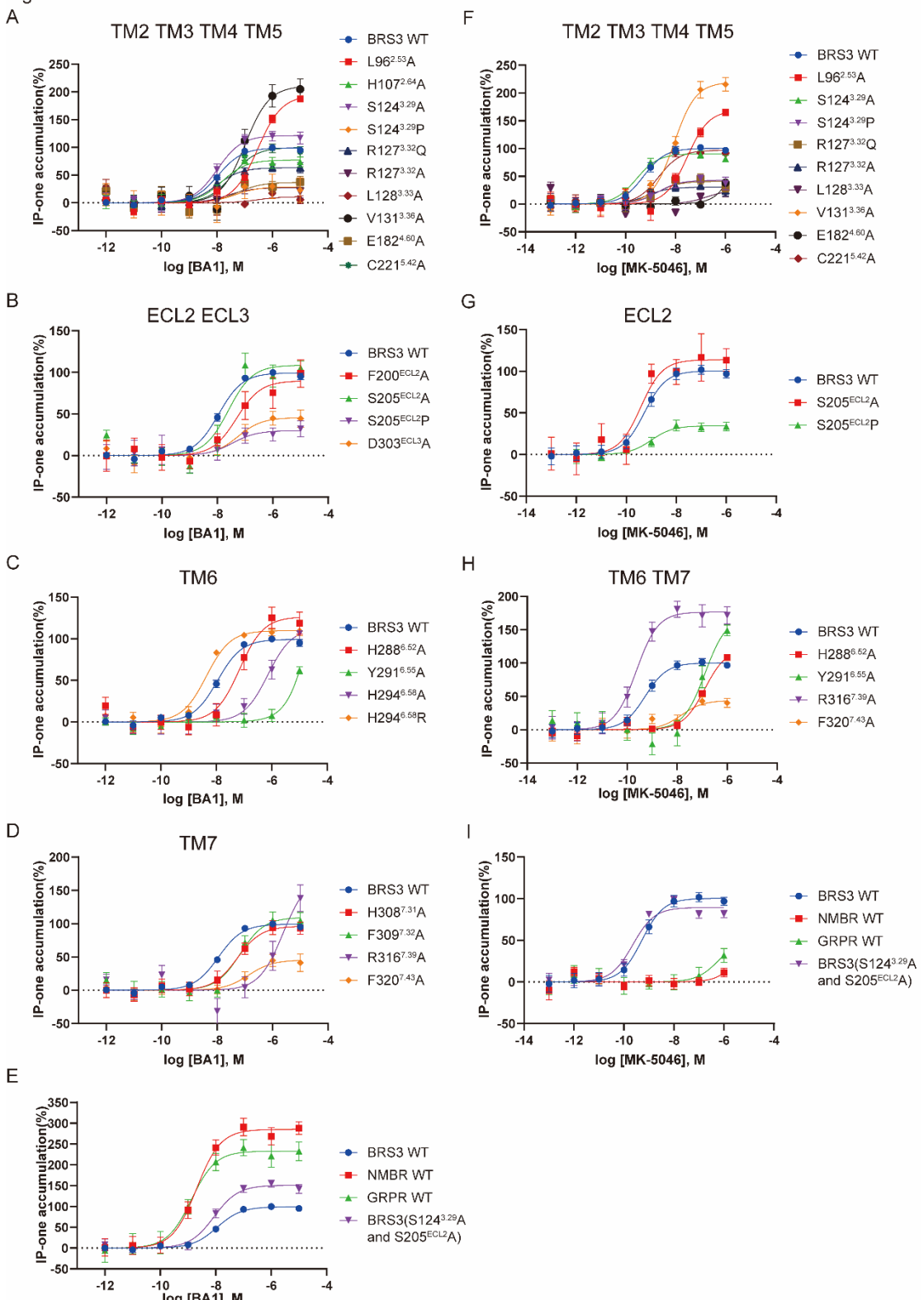
1307

1308

1309

1310

Figure S8



1311

1312

1313 **Figure S8. IP1 response curves of BA1 and MK-5046.** BRS3 mutations on agonists

1314 BA1 (A-E) and MK-5046 (F-I) induced signaling effects. Dose-response curves for

1315 ligands were performed in transiently transfected AD293 cells. The results are
1316 expressed as percentage of the maximal effect observed in BRS3 wild type. Wild-type
1317 and mutated BRS3 data are shown by different colors as figures. Each point represents
1318 the mean \pm S.E.M. of 3 to 7 independent experiments with triplicate determinations.

1319

1320

1321

1322

1323

1324

1325

1326

1327

1328

1329

1330

1331

1332

1333

1334

1335

1336

1337

1338

1339

1340

1341

1342

1343

Figure S9

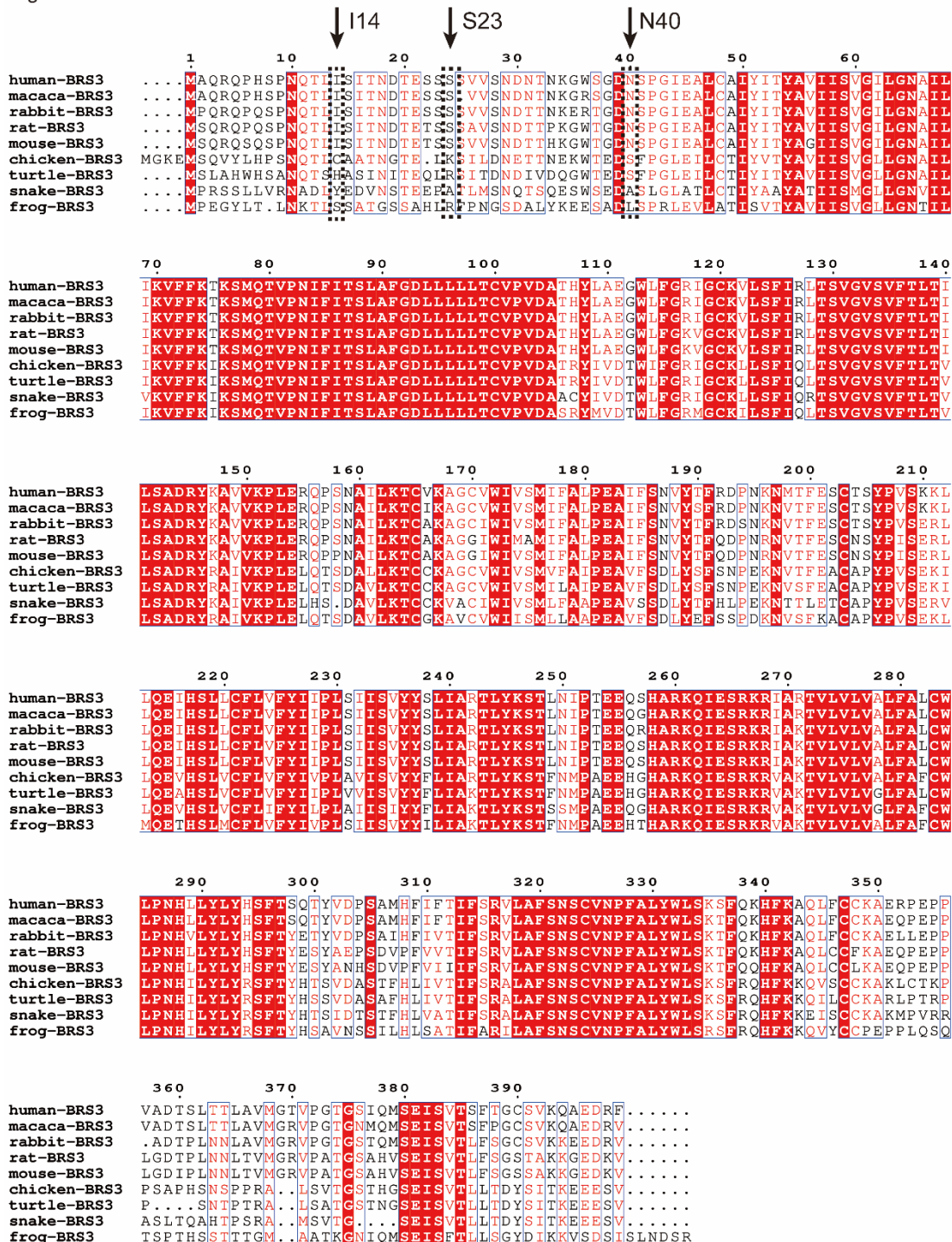


Figure S9. Sequence alignment of BRS3 of different species including placental mammals (human, macaca mulatta, rabbit, rat, and mouse) and non-placental vertebrates (chicken, turtle, snake, and frog).

1350 **Table S1.** The affinity(pK_i) data of Bn-related ligands for human bombesin receptor
1351 family.

	pK_i^*			
	NMB	GRP(14-27)	BA1	MK-5046
hNMBR	8.1-10.3	6.8-6.9	7.8-9.7	<5.0
hGRPR	7.7-7.8	9.7-9.8	7.8-8.0	<5.0
hBRS3	5.7	<5.0	8.1-8.4	7.7-8.4

*The data are from the website "<https://www.guidetopharmacology.org/>".

1352

1353

1354

1355

1356

1357

1358

1359

1360

1361

1362

1363

1364

1365

1366

1367

1368

1369

1370

1371

1372

1373

1374

1375

Table S2. Cryo-EM data collection, model refinement and validation statistics.

	apo BRS3-G _q -scFv16 complex	BA1-bound BRS3-G _q complex	MK-5046-bound BRS3-G _q -scFv16-Nb35 complex
Data collection and processing			
Detector	K3	K3	Falcon 4
Magnification	64,000	105,000	165,000
Voltage (kV)	300	300	300
Electron exposure (e ⁻ /Å ²)	50	50	50
Defocus range (μm)	-1.0~3.0	-1.0~3.0	-1.0~3.0
Pixel size (Å)	1.08	0.824	0.73
Symmetry imposed	C1	C1	C1
Initial particle projections (no.)	3,294,877	6,245,406	3,416,175
Final particle projections (no.)	233,381	675,060	196,746
Map resolution (Å)	3.3	2.90	2.93
Map resolution range (Å)	2.60-4.40	2.40-4.20	2.40-4.20
FSC threshold	0.143	0.143	0.143
Model Refinement			
Refinement package	PHENIX-1.17.1-3660	PHENIX-1.17.1-3660	PHENIX-1.17.1-3660
Real or reciprocal space	Real space	Real space	Real space
Model-Map CC (mask)	0.43	0.63	0.62
Model resolution (Å)	3.30	2.87	3.70
FSC threshold	0.143	0.143	0.5
B factors (Å ² , min/max/mean value)			
Protein residues	22.81/126.95/65.54	20.00/126.95/64.51	22.81/155.34/71.34
Ligands	-/-	20.00/20.00/20.00	20.00/20.00/20.00
Model composition			
Non-hydrogen atoms	9,067	7,380	10,071
Protein residues	1,153	930	1,281
R.m.s. deviations			
Bond lengths (Å)	0.001	0.003	0.003
Bond angles (°)	0.386	0.649	0.924
Validation			
MolProbity score	1.24	1.26	1.19
Clashscore	4.70	5.01	4.09
Rotamer outliers (%)	0.10	0.25	0.09
Ramachandran plot			
Favored (%)	98.59	98.47	98.42
Allowed (%)	1.41	1.53	1.58
Disallowed (%)	0.00	0.00	0.00
Data availability			
EMDB entry	EMD-38927	EMD-38928	EMD-38929
PDB entry	8Y51	8Y52	8Y53

1376

1377

1378

1379

1380

1381

Table S3. Sequence of Bn-related peptides used or mentioned in this study.

Peptide name	N-Terminus	position relative to Bn													
		1	2	3	4	5	6	7	8	9	10	11	12	13	14
Endogenous															
Bn(Bombesin)		pE	Q	R	L	G	N	Q	W	A	V	G	H	L	M-NH ₂
GRP27(GRP(1-27))	VPLPAGGGTVLTK	M	Y	P	R	G	N	H	W	A	V	G	H	L	M-NH ₂
GRP (14-27)a(GRP (14-27))		M	Y	P	R	G	N	H	W	A	V	G	H	L	M-NH ₂
GRP (14-27)b(GRP (14-27))		M	Y	P	R	G	N	H	W	A	V	G	H	L	M
NMB(Neuromedin B)						G	N	L	W	A	T	G	H	F	M-NH ₂
NMB30(Neuromedin B (1-30))	LSWDLPEPRSASKIR	V	H	R	R	G	N	L	W	A	T	G	H	F	M-NH ₂
NMC(Neuromedin C)						G	N	H	W	A	V	G	H	L	M-NH ₂
Exogenous															
BA1([D-Phe ⁶ ,β-Ala ¹¹ , Phe ¹³ ,Nle ¹⁴]bombesin-(6-14))						D	F	Q	W	A	V	βA	H	F	X
						1	2	3	4	5	6	7	8	9	10
															position relative to NMB or NMC

1382

1383

1384

1385

1386

1387

1388

1389

1390

1391

1392

1393

1394

1395

1396

1397

1398

1399

1400

1401

1402

1403

1404

1405 **Table S4. Ligand binding affinities and expression levels of WT and mutated**
1406 **BRS3.** The wild type (WT) and mutants of BRS3 discussed in this manuscript were
1407 individually analyzed. The affinities are derived from at least 3 independent
1408 experiments using IP1 function assay. The expression level of mutant BRS3 were
1409 normalized to wild-type BRS3 as 100%, respectively. Each data point represents mean
1410 \pm standard error of the mean (S.E.M.). All data were analyzed by two-sided Student's t
1411 test. *P<0.05, **P<0.01, ***P<0.001 vs. WT. Source data are available online.
1412 Definitions: NA – not applicable; NT, not tested.

1413

Residue Number	BRS3 mutants	Expression (% of WT)	BA1 pEC ₅₀ ±S.E.M.	BA1 ±S.E.M.(%WT)	E _{max}	MK-5046 pEC ₅₀ ±S.E.M.	MK-5046 E _{max} ±S.E.M.(%WT)
-	WT	100±0.60	-7.81±0.10	98.95±0.93	-9.3±0.08	99.61±5.08	
2.53	L96A	56.14±0.57	-6.53±0.06***	194.35±2.50***	-7.51±0.08**	169.55±5.24***	
2.64	H107A	49.66±2.25	-7.82±0.08	77.26±15.79*	NT	NT	
3.29	S124A	88.27±0.52	-7.98±0.03	121.41±17.26*	-9.52±0.12	99.31±31.63	
3.29	S124P	46.96±0.90	-7.83±0.20	3.33±5.12***	-8.45±0.47	47.27±11.52***	
3.32	R127A	78.5±1.49	-7.5±0.23	27.57±18.50***	-9.12±0.25	30.09±4.74***	
3.32	R127Q	88.55±1.84	-8.06±0.11	63.09±13.39***	-9.06±0.16	53.85±10.57**	
3.33	L128A	69.71±1.14	NA	NA	NA	NA	
3.36	V131A	49.89±1.91	-6.98±0.06**	211.09±33.36***	-8.04±0.15	220.25±26.06***	
4.60	E182A	63.43±2.10	-7.13±0.06**	74.21±5.15***	-4.93±3.56*	NA	
ECL2	F200A	51.62±1.89	-6.98±0.79	110.6±38.69	NT	NT	
ECL2	S205A	61.14±0.37	-7.59±0.10	109.11±18.74	-9.46±0.14	100.42±6.74	
ECL2	S205P	119.29±0.27	-7.33±0.12*	30.57±14.93***	-9.06±0.34	34.47±8.97***	
5.42	C221A	40.62±0.58	-7.38±0.18	129.13±23.94*	-8.67±0.21	96.99±4.55	
6.52	H288A	34.09±0.29	-7.14±0.15**	127.01±18.88*	-6.9±0.07***	NA	
6.55	Y291A	93.13±0.58	-5.22±0.12***	NA	-6.77±0.21***	NA	
6.58	H294A	94.44±1.20	-6.15±0.16***	114.14±13.68*	NT	NT	
6.58	H294R	76.83±1.04	-8.34±0.11*	110.1±7.27*	NT	NT	
ECL3	D303A	60.11±1.58	-7.34±0.28	45.94±16.74***	NT	NT	
7.31	H308A	82.8±0.17	-7.31±0.27*	97.07±17.95	NT	NT	
7.32	F309A	98.74±2.23	-7.17±0.06**	109.52±24.06	NT	NT	
7.39	R316A	33.25±0.30	-5.88±0.04***	NA	-9.62±0.04	176.84±25.63***	
7.43	F320A	43.75±1.26	-6.87±0.07***	45.31±5.73***	-8.49±0.58	40.28±5.61***	
3.29, ECL2	S124A, S205A	14.41±0.08	-8.06±0.04	151.15±13.19***	-9.65±0.11	89.3±3.87	
NMBR-WT		73.17±2.73	-8.66±0.11**	285.63±35.44***	NA	NA	
GRPR-WT		42.71±0.73	-8.85±0.10***	200.2±37.77***	NA	NA	

1414

1415

1416

1417

1418

1419

1420

1421 **Table S5. Sequence alignment of the key residues in sodium site, DRY motif,**
 1422 **PV(I)F motif, toggle switch and NPxxY motif, as well as residues involved in**
 1423 **disulfide bond formation in bombesin receptors.**

	Sodium site		Disulfide bond			DRY motif			PV(I)F motif			toggle switch			NPxxY motif		
Residue position	2.50	3.39	3.25	4.64	5.34	3.49	3.50	3.51	5.50	3.40	6.44	6.44	6.48	7.43	7.49	7.50	7.54
NMBR	D	S	C	T	H	D	R	Y	P	V	F	F	W	F	N	P	Y
GRPR	D	S	C	S	H	D	R	Y	P	V	F	F	W	F	N	P	Y
BRS3	D	S	C	S	L	D	R	Y	P	V	F	F	W	F	N	P	Y
Class A conserved	D	S	C	x	x	D	R	Y	P	V(I)	F	F	W	F/Y	N	P	Y

1424

1425

1426

1427

1428

1429